Mapping the strain-stiffening behavior of the lung and lung cancer at microscale resolution using the crystal ribcage

Robert LeBourdais[1]†, **Gabrielle N. Grifno**[1], **Rohin Banerji**[1], **Kathryn Regan**[1], **Bela Suki**[1], **and Hadi T. Nia**[1,*]
Department of Biomedical Engineering, Boston University, Boston, MA, USA

*** Correspondence:**
Hadi T. Nia, Ph.D.
htnia@bu.edu

Keywords: Crystal ribcage, elastography, multiscale modeling, ex vivo, finite-element analysis, remodeling, cancer, strain-stiffening.

Abstract

Lung diseases such as cancer substantially alter the mechanical properties of the organ with direct impact on the development, progression, diagnosis, and treatment response of diseases. Despite significant interest in the lung's material properties, measuring the stiffness of intact lungs at sub-alveolar resolution has not been possible. Recently, we developed the crystal ribcage to image functioning lungs at optical resolution while controlling physiological parameters such as air pressure. Here, we introduce a data-driven, multiscale network model that takes images of the lung at different distending pressures, acquired via the crystal ribcage, and produces corresponding absolute stiffness maps. Following validation, we report absolute stiffness maps of the functioning lung at microscale resolution in health and disease. For representative images of a healthy lung and a lung with primary cancer, we find that while the lung exhibits significant stiffness heterogeneity at the microscale, primary tumors introduce even greater heterogeneity into the lung's microenvironment. Additionally, we observe that while the healthy alveoli exhibit strain-stiffening of ~1.75 times, the tumor's stiffness increases by a factor of 6 across the range of measured transpulmonary pressures. While the tumor stiffness is 1.4 times the lung stiffness at a transpulmonary pressure of 3 cmH_2O, the tumor's mean stiffness is nearly five times greater than that of the surrounding tissue at a transpulmonary pressure of 18 cmH_2O. Finally, we report that the variance in both strain and stiffness increases with transpulmonary pressure in both the healthy and cancerous lungs. Our new method allows quantitative assessment of disease-induced stiffness changes in the alveoli with implications for mechanotransduction.

1 Introduction

Altered stiffness is one of the four physical hallmarks of cancer[1,2], with implications for the development, progression, diagnosis, and treatment response of solid cancers. Biologically, elevated stiffness promotes proliferation[3], invasiveness[4], and metastasis[5] through activation of mechanosensitive signaling pathways; clinically, an increase in stiffness is associated with an increased risk of breast cancer[6] and mortality.[7] In diagnostics, cellular and extracellular stiffness are traditional markers of cancer[8,9] and are predictive of a tumor's stage.[10] In therapy, increased stiffness is linked to reduced efficiency of drug delivery.[11] Furthermore, determining the stiffness

of the tumors and their surrounding tissue is an essential precursor for estimating solid mechanical stresses, another physical hallmark of cancer.[2,11-15] Despite this, the lung's or a lung tumor's stiffness has not been reported under the following conditions: (i) across a range of physiologically relevant pressures, (ii) noninvasively, i.e., without sectioning of the tissue, (iii) under realistic boundary conditions, and (iv) at microscale resolution.

Although elastography encompasses a broad range of techniques for assessing the material properties of biological tissues, each method presents limitations when addressing our specific problem.[7,9,16-25] The gold-standard method for microscale elastography is atomic-force microscopy[26], which boasts extremely high-resolution, absolute measurements of stiffness. However, tissue preparation for AFM involves resection and submersion in saline, which disrupts the mechanical integrity of the sample and the alveolar air-liquid interface.[27] Though CT and MRI elastography preserve the mechanical environment of the organ, these methods have poor spatiotemporal resolution, and they typically report strain rather than absolute stiffness.[28,29] Although strain elastography based on modalities like synchrotron microCT[30] have near-micron spatial resolution, to our knowledge, these methods lack the control and temporal resolution needed for tracking the same region of interest at alveolar resolution across changes in inflation pressure. Optical elastography[21,25,31] offers an alternative method for more precisely estimating the displacements throughout a biological sample. For example, recent papers have implemented optical elastography based on digital image correlation (DIC) to quantify the lung's strain[32] and stiffness;[33] but in each case, the empirical method does not provide physiologically realistic boundary conditions, and the measurements are not at alveolar resolution. Using optical elastography based on deformable image registration, our group recently mapped the elasticity of resected biological samples at optical resolution either by embedding them in thermo-responsive hydrogels[34] or by adhering precision-cut lung slices.[35] However, these methods also involve resection of the organ and embedding the sample in saline, which does not preserve the organ's boundary conditions and disrupts the air-liquid interface in the lung.

With that goal in mind, we recently developed the crystal ribcage[36], which preserves the integrity of the organ and emulates the *in vivo* boundary conditions seen by the lung, while at the same time enabling real-time microscopy of the entire surface during dynamic ventilation at cellular resolution (Fig. S1). Unlike intravital imaging methods[37-39] wherein the lung is immobilized by vacuum or glue, and which thus compromise the breathing mechanics of the lung at the imaging site, the plasma-treated crystal ribcage provides a lubricious, geometrically realistic boundary condition, allowing mechanical characterization of the lung throughout the breathing cycle in health and disease. While the tissue preparation involves resection of the organ from the mouse's thorax, the *ex vivo* lung, with its pleura intact, is imaged immediately after resection, and the lung can be vascularly perfused with complete media to maintain cell health throughout the course of imaging. Consequently, our platform preserves the *in vivo* physiological conditions of the lung. By developing an optical elastography platform based on the crystal ribcage apparatus, we can assess the mechanical properties of the *ex vivo* lung in health and disease with high spatiotemporal resolution and with physiologically realistic boundary conditions.

Here, to accurately estimate the *in vivo* mechanical properties of the lung in health and disease, we adopt a multiscale-modeling approach that couples the microscale displacements estimated through deformable image registration and the mean, strain-dependent stiffnesses estimated using

a nonlinear, finite-element model of the lung. We validate the multiscale model against a virtual, finite-element model of the lung with a cancerous tumor, demonstrating that the method is capable of accurately recovering the mechanical properties throughout the domain even in the presence of pathology. Upon applying the model to images of the lung within the crystal ribcage, we find that (i) the stiffness of the lung tissue increases nonlinearly with transpulmonary pressure across the full range of end-expiratory to end-inspiratory pressures; (ii) there is significant heterogeneity in material properties at alveolar resolution; (iii) the intratumor stiffness increasingly exceeds the extratumor stiffness across the entire range of pressures; and finally, (iv) the variance in stiffness increases with strain for both the healthy and cancerous tissue. While the present study characterizes the micromechanics of the healthy lung and the lung with cancerous tumors, the method has the potential to be applied to a wide range of disease states such as fibrosis, COPD, and respiratory infections.

2 Methods

2.1 Mouse model of lung cancer, crystal ribcage fabrication, and imaging

2.1.1 Animal use ethics

All experiments conformed to the ethical principles and guidelines under protocols set forth and approved by the Boston University Institutional Animal Care and Use Committee (protocol number PROTO201900086). All animal procedures were compliant with ARRIVE guidelines. Mice were housed in ambient temperature and humidity and 12-hour light–dark conditions under pathogen-free conditions at the Boston University Animal Science Center. No housing or handling exceptions were made for this study.

2.1.2 Mice

We used 11- to 23-week-old male and female mice for experimental procedures including healthy lung imaging and generating models of primary cancer, as previously described[36]. A breeding pair of transgenic B6.129(Cg)-Gt(ROSA)26Sortm4(ACTB-tdTomato,-EGFP)Luo/J (JAX, 007676, Jackson Labs)[40], referred to by the abbreviation "mTmG", was initially purchased to breed a colony; that colony was the source of all animals for healthy lung and primary cancer experiments. For the present study, which examines two representative mice from this colony, the healthy mouse was 11 weeks old at the time of imaging. The urethane mouse, serving as our model of primary cancer, was 23 weeks at the start of urethane dosing and 54 weeks at the time of imaging. Between these ages, the murine lung's volume does not change appreciably both in our experience and per development studies.[41]

2.1.3 Primary cancer model

We adapted a previously described protocol[42,43] to induce primary lung cancer in mTmG mouse lungs using urethane (Sigma U2500). A stock solution of urethane was prepared at a working concentration of 200 mg/mL in PBS. Mice were dosed with the urethane solution at 1 mg/g body weight, twice weekly for 5 weeks by intraperitoneal (IP) injection. Mice were sacrificed and lungs harvested for imaging in the crystal ribcage after 6-12 months. The maximum tumor size permitted

for the study was 1.5 mm in diameter. Mice were excluded from the study after presenting with labored breathing, hunched posture, or ruffled fur due to tumor progression.

2.1.4 Crystal ribcage fabrication

The full development of the crystal ribcage platform is described in our previous work.[36] Briefly, microCT scans of C57BL/6 mouse chest cavity (courtesy the Hoffman group at the University of Iowa[44-46]) were segmented and refined to create the native ribcage geometry. In successive additive manufacturing and fabrication steps the ribcage model was converted into the crystal ribcage mold that was thermoformed over to create the polystyrene crystal ribcage. The internal surface was engineered to be hydrophilic to allow the lung to glide over its surface, as in the native ribcage. A six degree of freedom arm was included to rotate the crystal ribcage about any axis to image across the entire the distal lung surface using either a top-down or bottom-up configured microscope. Because lung volume changes significantly with age,[41] we have fabricated different, age-specific crystal ribcages to accommodate lungs of different sizes.[36]

2.1.5 Lung preparation

Isolated mouse lungs were ventilated and perfused as previously described[36,47]. Briefly, the mouse trachea was cannulated and the lungs dynamically ventilated (Kent Physiosuite Mouse Ventilator, Kent Scientific). The lungs were perfused by cannulating the pulmonary artery and left atrium, and perfusing serum-free RPMI cell culture medium (Corning) through the lung vasculature. After cannulating the trachea and mouse heart, the lung–heart block was excised and placed into the crystal ribcage for ex vivo microscopy under variable quasi-static positive air pressures.

2.1.6 Lung microscopy

As previously described[36], *ex vivo* lungs, under quasi-static inflation conditions and within the crystal ribcage, were imaged using (i) an upright Nikon stereomicroscope with a 1x objective, and (ii) an upright Nikon CSU X1 spinning-disk confocal microscope with 1x, 2x, 4x and 10x objectives, using NIS-Elements acquisition software and with the environmental temperature control set to 37 °C.

Z stacks of the diseased and healthy lungs were acquired on the confocal microscope using a 561 nm laser at 20-50 ms exposure (50-20 frames per second) per frame. Voxel sizes varied based on objective used, with XY resolution varying from 1-10 μm and Z step sizes varying from 2.5-12.5 μm. Total Z stack acquisition time was on the order of 6-15 seconds for each positive-end expiratory pressure (PEEP) condition.

Before imaging, lungs were gradually recruited by slowly raising the intratracheal pressure to 18 cmH_2O, measured using custom sensors sensitive to 0.1 cmH_2O, using a water column. The pressure was then reduced in decrements of 1 cmH_2O down to 2 cmH_2O. To allow the lung to relax to its steady-state condition, each pressure was maintained for 1 minute before imaging.

2.2 Organ-scale geometry modeling

Fig. 1 summarizes the multiscale model. In short, we (i) segment microCT images of the lung in MATLAB 2022b (The MathWorks, Inc.), (ii) construct a geometric model from the segmentation in SolidWorks 2021 (Dassault Systèmes), (iii) simulate ventilation of the organ-scale model in

Abaqus 2022 (Dassault Systèmes) for a range of material coefficients, (iv) determine the coefficients that optimally reproduce the observed pressure-distension behavior of the lung in the crystal ribcage, (v) solve the inverse elasticity problem for the distribution of material properties throughout the microscale domain in arbitrary units, and finally, (vi) rescale these relative stiffnesses so that the mean value matches the stiffness of the organ-scale model, yielding or goal of recovering the absolute stiffnesses throughout the microscale domain. Given a three-dimensional microCT image[44-46] of the mouse thorax, we first construct three-dimensional geometric models (Fig. 1(a)) of the mouse lung and ribcage for finite-element analysis as follows.

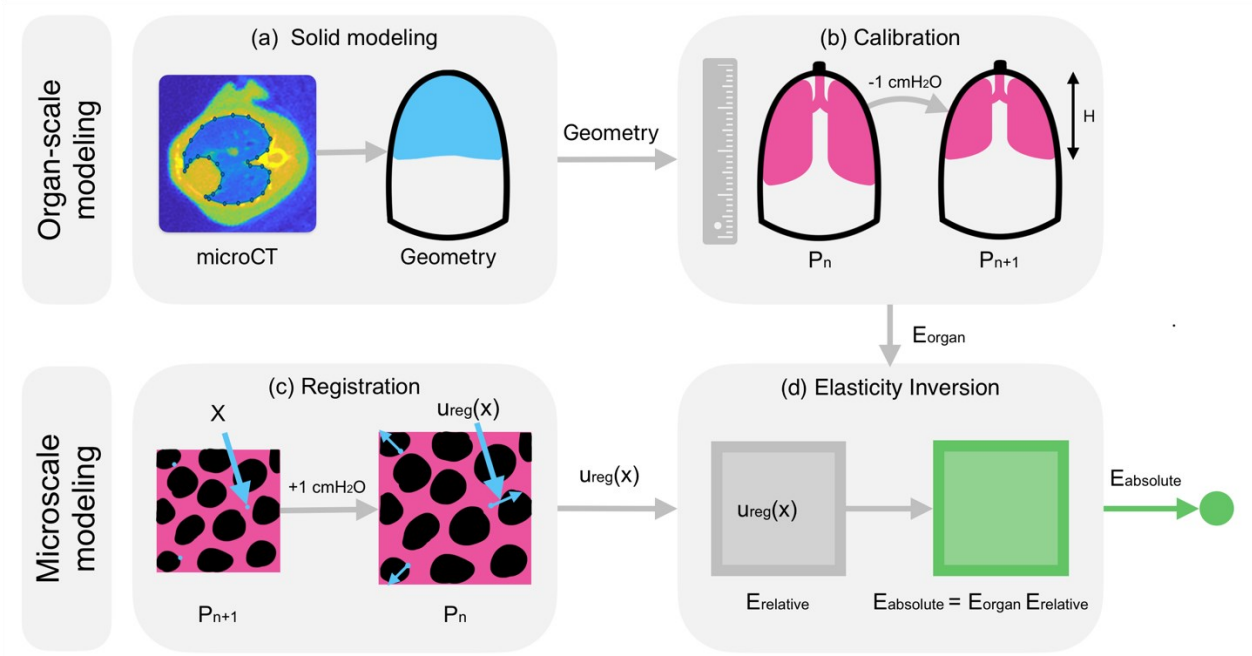

Figure 1 | Model description. (a) A Bayesian classifier segments the geometries of the lung and of the ribcage from microCT images[44-46] of the mouse thorax, and the segmentation is then used to construct a solid geometry in SolidWorks for finite-element analysis. (b) After recruitment, the height, H, of the organ in the crystal ribcage is measured as the distending transpulmonary pressure decreases from 18 to 2 cmH_2O in decrements of 1 cmH_2O, with the pressure at the start of the n^{th} step denoted by P_n, and the material constants of the finite-element model are chosen to reproduce this pressure-distension curve. (c) Deformable image registration determines how material points, x, within the lung tissue displace with microscale resolution in response to an increment in pressure of 1 cmH_2O, producing the estimated displacements, $u_{reg}(x)$, for that step, and (d) the inverse elasticity problem is solved using an implementation of the Adjoint-Weighted Equation formulation[48] of the inverse elasticity problem in Fenics,[49] an open-source Python framework for numerically solving differential equations in scientific computing applications. From the measured displacements, we recover an estimate of the elastic modulus in relative units, E_{relative}, having unity mean. Upon rescaling this estimate so that its mean value matches that of the organ-scale model, E_{organ}, we recover the absolute stiffness throughout the microscale domain, E_{absolute}.

2.2.1 Segmenting the lung and ribcage

Due to significant variations in the lung's intensity within a microCT volume, segmenting the organ by thresholding is unreliable. Consequently, we construct a naïve, Bayesian classifier—trained on a single, two-dimensional slice of the image along with its ground-truth class labels—to differentiate the lung class L from its surroundings M.[50] Let $\Omega \subset \mathrm{R}^3$ be the position vectors of pixels within the domain of the microCT image[44-46], so that $\vec{x} \in \Omega$ is the position of a given voxel.

The image can then be expressed as the scalar field $I(\vec{x}) : \Omega \to R$. Let $F(\vec{x}) : \Omega \to R^n$ map from each of these position vectors to the n-dimensional feature vectors extracted from $I(\vec{x}) : \Omega \to R$. In the present study, each feature vector has ten components, $\varphi_i(\vec{x}) : \Omega \to R$, each corresponding to a transformation of the image volume by a different neighborhood operation. These components are listed in Table 1.

Table 1 | Components of the feature vectors extracted from the microCT volume for building the Bayesian classifier. Each feature vector has ten components, each corresponding to a different transformation of the image volume. To normalize the components, each component is divided by its standard deviation.

Feature-vector component	Description
φ_1	Sobel filter with threshold 0.1 applied to I
φ_2	Sobel filter with threshold 0.4 applied to I
φ_3	Gaussian filter of variance 2 applied to φ_1
φ_4	Gaussian filter of variance 4 applied to φ_2
φ_5	Laplacian-of-Gaussian filter applied to I
φ_6	Gaussian filter of radius 4 applied to I
φ_7	Gaussian filter of radius 8 applied to I
φ_8	Gaussian filter of radius 16 applied to I
φ_9	The original image I
φ_{10}	Morphological dilation of φ_2

Let $\Omega_{\mathrm{L}} \subset \Omega$ be the subset of position vectors from a given slice of the image volume that have been manually labeled as belonging to the lung, and let $\Omega_{\mathrm{M}} \subset \Omega$ be the remaining position vectors from the same slice. For the priors, we assume that the prior probability $P(L) = \frac{|\Omega_L|}{|\Omega_L|+|\Omega_M|}$, which implies by the axiom of normalization that $P(M) = 1 - P(L)$. To estimate the likelihoods, $P(\vec{x} \mid L)$ and $P(\vec{x} \mid M)$, we train Gaussian mixture models on the feature vectors $F(\Omega_L)$ and $F(\Omega_M)$, respectively. Finally, from these definitions, we apply Bayes' theorem to recover $P(L \mid \vec{x})$, the posterior probability that a given pixel belongs to the lung.

$$(1) \qquad P(L \mid \vec{x}) = \frac{P(\vec{x} \mid L)P(L)}{P(\vec{x} \mid L)P(L) + P(\vec{x} \mid M)P(M)}$$

The lung segmentation $S_L(\vec{x}): \Omega \to \{0,1\}$ is then defined as $S_L(\vec{x}) = 1$ if $P(L \mid \vec{x}) > 0.5$ and $S_L(\vec{x}) = 0$ otherwise. In the MATLAB implementation, these maps—$I(\vec{x}), F(\vec{x}), S_L(\vec{x})$, and $P(L \mid \vec{x})$—are represented as matrices.

In contrast, the ribcage segmentation $S_R(\vec{x}): \Omega \to \{0,1\}$ is defined as $S_R(\vec{x}) = 1$ if and only if the intensity $I(\vec{x})$ exceeds some constant, volume-dependent threshold. In each case, the resulting segmentation contains multiple connected components, corresponding to features like the scapula, humerus, cartilaginous tracheal rings, and tissue outside of the lung; extracting the largest connected components from these initial segmentations isolates the desired region of interest.

2.2.2 Constructing solid models of the lung and ribcage

From the lung segmentation $S_L(\vec{x})$, we approximate the surface of the diaphragm as follows. First, we find $z_{\max}(x, y) = \max \{ z \mid (x, y, z) \in \mathrm{Dom}(S_L) \wedge S_L(x, y, z) = 1 \}$. We then filter the mapping

$z_{\max}(x, y)$ using a mode filter. Finally, we resample points from this surface using a thin plate smoothing spline and save the point cloud to a text file.[51]

To construct a point-cloud approximation of the ribcage, we then find the geometric centroid of the lung, $\vec{x}_c$, from $S_L(\vec{x})$ using the following equation.

$$\vec{x}_c = \frac{1}{\sum_{\vec{x}\in\Omega} S_L(\vec{x})} \sum_{\vec{x}\in\Omega} \vec{x}\, S_L(\vec{x}) \quad (2)$$

For each slice of the volume, we then project rays from the projection of the centroid $\vec{x}_c$ onto the given slice at a dense collection of angles from 0 to 2π until each ray contacts a nonzero pixel on the interior of the ribcage segmentation $S_R(\vec{x})$. A thin plate smoothing spline is then fit to these contact points to produce a surface approximating the ribcage, and a dense collection of points, P_R, are sampled from this surface. Because the ribcage is open near the apex of the lung, these sampled points are artifactually peaked in the neighborhood of the apex. To correct this, the nodes near the apex are flattened by minimizing the following objective function.

$$\sum_i (k(z_i - Z_i) - g_z)^2 + \alpha\left(\nabla_{xy} z_i\right)^2 + \beta\left(\nabla_{xy}^2 z_i\right)^2 + \gamma\left(\nabla_{xy}(z_i - Z_i)\right)^2 + \delta\left(\nabla_{xy}^2 (z_i - Z_i)\right)^2 \quad (3)$$

In this equation, z_i represents the z-component of the i[th] node's position vector after correction, Z_i represents the same component before correction, k represents the stiffness of a virtual spring anchoring a point to its original height, and g_z is a body force pulling these points toward the centroid of the ribcage. The remaining terms serve to regularize the optimization, penalizing the first and second derivatives of the height as well as changes in these derivatives. The sum is taken over the points near the apex of the lung. Finally, these point clouds of the lung and ribcage are saved as text files for subsequent import into SolidWorks.

From these point clouds, we finally construct STEP (Standard for the Exchange of Product model data defined by ISO 10303[52]) representations of the ribcage and the diaphragm using the ScanTo3D feature in SolidWorks. By cutting the ribcage surface with the diaphragm surface, and filling the space enclosed between them, we recover a simplified model of the lung that is everywhere tangent to the ribcage. The STEP representations of the ribcage and the lung are then exported from SolidWorks.

2.3 Organ-scale finite-element modeling

2.3.1 Simulating the healthy lung

To perform finite-element simulations of the organ, these STEP geometries are now imported into Abaqus 2022 (Dassault Systèmes). The ribcage is taken to be a discrete, rigid part and is meshed with rigid, triangular elements. The lung is taken to be a deformable part and is meshed with C3D10 quadratic tetrahedral elements, which are chosen over C3D4 linear tetrahedral elements for their tendency to converge more quickly with coarser mesh resolutions. In simulations of the healthy lung, the lung mesh consists of 34,541 nodes and 21,945 elements; the ribcage mesh consists of 64,093 nodes and 127,697 elements. The simulation was performed on the Boston

University Shared Computing Cluster hosted by the Massachusetts Green High-Performance Computing Center distributing the load over 12 processors with 4 GB of RAM per processor, each simulation completed within 7 hours.

Based on prior studies and on the lung's microstructure and constitutive behavior—which resembles a hyperelastic, tetrakaidekahedral foam whose walls are comprised of elastin, type-I collagen, and type-III collagen—the lung is modeled using the Ogden-Hill model[53] of a hyperelastic foam.[54,55] The general form of the strain-energy density function is thus taken to be

$$U = \sum_{i=1}^{N} (2\mu_i/\alpha_i^2)(\lambda_1^{\alpha_i} + \lambda_2^{\alpha_i} + \lambda_3^{\alpha_i} - 3 + \frac{1}{\beta_i}(J^{-\alpha_i\beta_i} - 1)), \quad (4)$$

where α_i is a dimensionless material parameter determining the nonlinear behavior of the stress-strain relation, β_i is a dimensionless material parameter given by the Poisson's ratio as $\beta_i = \nu_i/(1-2\nu_i)$, μ_i is a material parameter with units of stress determining the shear modulus during small strains from the reference configuration, λ_i is the i^{th} principal stretch, J is the determinant of the deformation gradient, and N is the number of terms in the model. For simplicity, we assume that the strain-energy density function consists of only one term, reducing the general equation to

$$U = (2\mu/\alpha^2)(\lambda_1^{\alpha} + \lambda_2^{\alpha} + \lambda_3^{\alpha} - 3 + \frac{1}{\beta}(J^{-\alpha\beta} - 1)). \quad (5)$$

This strain-energy density function, and consequently the pressure, is linear in the parameter μ and nonlinear in the parameter α. Therefore, if we simulate the distensions for parameters (μ, α), then the pressures required to produce the same distensions for any other (μ^*, α) are a simple rescaling of those for (μ, α). In practice, therefore, it is unnecessary to simulate ventilation for the same α but different μ to determine the pressure-distension curve.

The boundary conditions (Fig. S2) include immobilization of the ribcage, frictionless sliding contact between the lung's upper surface and the ribcage, and negative pressure on the boundary of the lung. Although experiments involve positive-pressure ventilation, the simulation involves applying negative pressure to the external surface of the lung; the explanation for this apparent discrepancy is that the governing equations are symmetric under mutual inversion of the pressure's sign and the surface normal's direction, implying that the model is equally applicable to either mode of ventilation.[56] Since the parts have been designed *a priori* to be tangent everywhere, initial contact between the surfaces is easy to establish.

While previous studies[56,57] have shown that gravity significantly influences the mechanics of the human lung, our model neglects the influence of gravity due to its smaller role in the mouse. Consider the conservation of linear momentum under conditions of static equilibrium, which has been rendered dimensionless[58] by factoring out the lung density ρ_{lung}, gravitational acceleration g, lung height H_{lung}, and transpulmonary pressure P_{tp}.

$$\frac{P_{\mathrm{tp}}}{\rho_{\mathrm{lung}} g H_{\mathrm{lung}}} \nabla^* \cdot P^* + B^* = 0 \quad (6)$$

Here, ∇^*, P^*, and B^* represent the dimensionless divergence operator, the dimensionless tissue stress, and the dimensionless gravitational body forces, respectively. The tissue stress is known to be approximately equal to the transpulmonary pressure.[59] Consequently, the dimensionless number $\frac{P_{\text{tp}}}{\rho_{\text{lung}} g H_{\text{lung}}}$ characterizes the magnitude of the tissue stress divergence relative to the magnitude of gravity. In the human lung, this dimensionless quantity remains below 1 for transpulmonary pressures up to 20 cmH_2O, indicating the significant role of gravity in governing its mechanics. In the mouse lung, however, this dimensionless quantity is equal to 1 when the transpulmonary pressure is 1 cmH_2O, but decreases linearly as the transpulmonary pressure increases; once the transpulmonary pressure reaches 10 cmH_2O, this dimensionless number increases to 10, indicating that tensile forces within the tissue greatly exceed gravitational body forces. Based on this reasoning, we posit that it is reasonable to neglect gravity when modeling the murine lung, with the approximation improving at higher pressures. Additional reasoning is discussed in the results.

Finally, it is important to note that the lung exhibits hysteresis, with its inflation characterized by one strain-energy density function and its deflation characterized by another.[55] In this study, we elect to model the lung's behavior during quasistatic deflation, so that our measurements used to calibrate the model are taken from states of higher pressure to states of lower pressure in near-equilibrium. The same approach can easily be repeated to recover a model of the lung's behavior during inflation.

2.3.2 Simulating the cancerous lung

To simulate the cancerous lung, the same process is repeated, but rather than being constant, the material field $\mu(\vec{X})$ is defined as

$$\mu(\vec{X}) = Ae^{-(\vec{X}-\vec{X}_{\text{tumor}})^n/\sigma^2} + B, \quad (7)$$

where $\vec{X}_{\text{tumor}}$ is the centroid of the spherical tumor in material coordinates, σ determines its width, n controls the shape of the decay in magnitude with distance, and the coefficients A and B determine the stiffness in the near and far fields. To illustrate, we note that $\mu(\vec{X})$ approaches $A + B$ as $\vec{X}$ approaches $\vec{X}_{\text{tumor}}$, and that $\mu(\vec{X})$ approaches B as $\|\vec{X} - \vec{X}_{\text{tumor}}\|$ approaches infinity. Consequently, $A + B$ is the stiffness at the tumor's centroid, while B is the stiffness far from the tumor. This material equation possesses three attractive properties: (i) it is spherically symmetric, corresponding to our interpretation that the equation represents a spherical tumor, (ii) stiffness decays with distance from the centroid, reflecting our intent that the tumor is stiffer than its surroundings, and (iii) it is differentiable and smooth, making it easier to work with during numerical computations. When $n = 2$, the field is a multidimensional normal distribution, and as $n \to \infty$, the field approaches an indicator function for a ball. In our studies, we chose $n = 4$.

The ribcage mesh is the same as before, while the lung mesh now consists of 12,679 nodes and 7,766 elements. Adaptive mesh refinement, which was necessary for convergence in the neighborhood of the tumor, yielded a mesh with fewer elements relative to the simulation of the healthy lung. The simulation was performed on the Boston University Shared Computing Cluster hosted by the Massachusetts Green High-Performance Computing Center; distributing the load over 12 processors with 4 GB of RAM per processor, the simulation completed within 4 hours.

2.3.3 Calibrating the organ-scale finite-element model

The finite-element simulation is repeated for different material parameters within a neighborhood of the values yielding optimal agreement between empirical and *in silico* outcomes. When the strain-energy density function is restricted to a single term, the parameter μ represents the material's shear modulus during small strains, as can be shown by a Taylor expansion of the strain-energy density function about $\lambda = 1$. From the stress-strain curve in the linear regime, when the strain increases linearly with distending pressure, we can estimate the Young's modulus as the ratio of the increment in strain to the increment in pressure. From Fig. 2(c), we estimate that incrementing the pressure from 0 kPa to 5 kPa yields an increment in strain of 0.2. Following this reasoning, we find that $E \approx 5\ \text{kPa}/0.2 = 2.5\ \text{kPa}$. Assuming a Poisson's ratio of $\nu = 0.2$,[60] this value for the Young's modulus corresponds to a shear modulus of $\mu = E/(2(1+\nu)) \approx 1\ kPa$.

Based on these initial estimates, we perform simulations for $\mu = 1$ kPa and the dimensionless parameter α ranging from 6 to 16. The outcomes of these simulations are then used to construct a calibration surface $P(\lambda_H, \mu, \alpha)$, where λ_H is the stretch of the finite-element model along the vertical axis, μ and α are the material parameters mentioned earlier, and P is the transpulmonary pressure required to distend the finite-element model to this degree of stretch. From the observed distensions of the lung in the crystal ribcage (Fig. 1(b)) for pressures ranging from 2 to 18 cmH_2O, (λ_{obs}, P_{obs}), we then determine the maximum likelihood assignments for μ and α by minimizing the following objective function.[50]

$$\sum_{(\lambda_{obs},P_{obs})}(P(\lambda_{obs},\mu,\alpha) - P_{obs})^2 \quad (8)$$

This optimization procedure is not computationally intensive; running on a personal laptop with 16 GB of RAM and a typical CPU, for example, the process completes within seconds. The outcome is a single, point estimate of the coefficients that characterize the organ-scale behavior. It should be noted that, because the model is linear in the parameter μ, we can in practice simplify the problem of determining the optimal parameters by transforming the objective function as follows.

$$\sum_{(\lambda_{obs},P_{obs})}(\mu P(\lambda_{obs},1,\alpha) - P_{obs})^2 \quad (9)$$

This implies that, rather than sampling the function $P(\lambda_{obs}, \mu, \alpha)$, we only need to sample the function $P(\lambda_{obs}, 1, \alpha)$ in our finite-element simulations. In contrast, because the model is nonlinear in α, an analogous transformation is not possible for α; this is why we limit the constitutive model to a single term.

2.4 Inverse elasticity problem at the microscale

2.4.1 Measuring the displacements using image registration

To measure the displacements caused by a change in distending pressure applied to the lung at cellular resolution, we leverage deformable image registration[61] (Fig. 1(c)). To prepare the images for registration, we perform an optimization to autonomously correct the bulk rotation of the material due to the natural curvature of the crystal ribcage away from the imaging plane. Because

the image-registration algorithm does not, in practice, yield good estimates for the displacements along the shallow depth axis, we project the rotationally corrected images along this axis.

After preprocessing the images, we invoke the image-registration algorithm. This algorithm, which has been adapted from earlier literature[61], formulates the inverse-elasticity problem as an inference problem on a Markov Random Field (MRF) to automatically determine the displacements necessary to match images of the lung at two different pressures. The observable variables of the Markov Random Field are modality-independent neighborhood descriptors (MIND) extracted from the image,[62] while the latent variables are the displacements necessary to minimize the sum of squared differences in these descriptors across the two images; edges between the latent variables of neighboring observables represent the constraint that displacements vary smoothly throughout the domain. Let $\boldsymbol{O}$ and $\boldsymbol{T}$ be the original and deformed images, respectively. Furthermore, let $W(\boldsymbol{O}, \boldsymbol{u})$ be the image produced by warping the image $\boldsymbol{O}$ using the displacements $\boldsymbol{u}$. Lastly, let the function D map an image to its MIND representation. Then the registration algorithm finds the displacements that minimize the objective function

$$\sum_{\vec{x}\in\Omega}\left(D\left(W(\boldsymbol{O},\boldsymbol{u})\right) - D(\boldsymbol{T})\right)^2, \tag{10}$$

where the sum is taken over the points in the image domain, Ω. From these displacements and the material properties of the calibrated finite-element model, we next find the distribution of stiffnesses throughout the domain, as described in the next section.

2.4.2 Solving for the shear modulus parameter

To determine the relative stiffnesses of the material throughout the image domain, we leverage a Python implementation of the Adjoint-Weighted Equation (AWE) formulation of the inverse-elasticity problem.[48] Let $\vec{X} \in \boldsymbol{\Omega_0} \subset \boldsymbol{R^2}$ be the coordinates of material points of a deformable body in the reference configuration, and let $\vec{x} \in \boldsymbol{\Omega_1} \subset \boldsymbol{R^2}$ be the coordinates of the same material points after some deformation. Because soft tissues deform continuously, there exists a continuous function $\boldsymbol{\psi} : \boldsymbol{R^2} \to \boldsymbol{R^2}$ such that $\vec{x} = \boldsymbol{\psi}(\vec{X})$. Given the registered displacements, $\boldsymbol{u}(\vec{X}) = \boldsymbol{\psi}(\vec{X}) - \vec{X}$, along with the definition of the deformation gradient, $\boldsymbol{F}(\vec{X}) = \nabla_{\vec{X}}\boldsymbol{\psi}(\vec{X})$, we can recover the deformation gradient tensor in terms of $\vec{X}$.[63]

$$\boldsymbol{F}(\vec{X}) = \boldsymbol{I} + \boldsymbol{\nabla}_{\vec{X}}\boldsymbol{u}(\vec{X}) \tag{11}$$

From the deformation gradient, we next determine the Cauchy-Green strain tensor field, $\boldsymbol{C}(\vec{X})$, as follows.

$$\boldsymbol{C}(\vec{X}) = \boldsymbol{F}(\vec{X})^{\boldsymbol{T}}\boldsymbol{F}(\vec{X}) \tag{12}$$

By the spectral theorem and the manifest symmetry of $\boldsymbol{C}(\vec{X})$, we subsequently determine the eigenvalues, $\lambda_1(\vec{X})^2$ and $\lambda_2(\vec{X})^2$, of this tensor.

The areal strain, which is a scalar field representing the fractional change in the material's area relative to its value in the reference configuration, is then given by

(13) $\varepsilon_A(\vec{X}) = \lambda_1(\vec{X})\lambda_2(\vec{X}) - 1.$

The whole organ's stress-strain behavior is well-described by a hyperelastic material law, where the nominal stress is the derivative of the strain-energy function with respect to the principal nominal stretches. If we assume that this model holds at all length scales, down to the cellular scale and for both healthy and diseased tissue, then we can use this same constitutive model when solving the inverse problem. Therefore, from the same strain-energy function introduced earlier, we recover the principal components of the first Piola-Kirchhoff stress tensor as follows.

(14) $P_i = \frac{\partial W}{\partial \lambda_i} = \mu(\vec{X})(\frac{2}{\alpha\lambda_i}(\lambda_i^{\alpha} - J^{-\alpha\beta}))$

where $\beta = \frac{\nu}{1-2\nu}$. In evaluating the above expression, we need to compute the Jacobian determinant $J = \lambda_1\lambda_2\lambda_3$, but image registration only yields the stretches tangential to the lung's surface. Consequently, we approximate J as $J \approx (\lambda_1\lambda_2)^{3/2}$. Finite-element simulations of the whole organ indicate that this approximation generally holds within 10-15% error (Fig. S2).

For a hyperelastic material, it is well-known that the eigenvectors of the stress are aligned with the eigenvectors of the strain. Therefore, if $\vec{v}_i$ are the principal directions of the right Cauchy-Green strain tensor, the first Piola-Kirchhoff stress tensor becomes

(15) $\boldsymbol{P} = P_1\vec{v}_1 \otimes \vec{v}_1 + P_2\vec{v}_2 \otimes \vec{v}_2.$

We can simplify the above expression by defining the tensor $\boldsymbol{A}(\vec{X}) = \boldsymbol{P}(\vec{X})/\mu(\vec{X})$, leading to the following simplified form.

(16) $\boldsymbol{P}(\vec{X}) = \mu(\vec{\mathrm{X}})\boldsymbol{A}(\vec{X})$

Here, $\mu(\vec{X})$ is unknown while $\boldsymbol{A}(\vec{X})$ is completely determined by the displacements. At static equilibrium and in the absence of body forces, the conservation of linear momentum requires that the divergence of the first Piola-Kirchhoff stress, $\boldsymbol{P}(\vec{X})$, with respect to the material coordinates, $\vec{X}$, vanishes.

(17) $\nabla_{\vec{X}} \cdot \boldsymbol{P}(\vec{X}) = 0$

From our earlier simplified form for $\boldsymbol{P}(\vec{X})$, the condition of static equilibrium becomes

(18) $\nabla_{\vec{X}} \cdot (\mu(\vec{X})\boldsymbol{P}(\vec{X})) = 0.$

In the AWE formulation of the inverse elasticity problem for a linearly elastic material, we seek a variational solution for $\mu(\vec{X})$ to the above differential equation. This yields a map $\mu(\vec{X})$ of relative stiffnesses, whose scale is determined by the specified-mean boundary condition.[64] After solving

the inverse problem for $\mu(\vec{X})$, we rescale $\mu(\vec{X})$ so that the mean stiffness throughout the domain matches the organ-scale stiffness determined by calibrating the finite-element model.

From Holzapfel's equation (6.180)[63], which is reproduced below as equation (19), along with the strain-energy function mentioned earlier, we determine the components of the elasticity tensor, $\mathbb{C}$, at each state of deformation for each position within the domain. In the following equation, S_a Pare the principal values of the second Piola-Kirchoff stress tensor, λ_a are the principal stretches, and $\hat{N}_a$ are the principal directions of the deformation.

$$\mathbb{C} = \sum_{a,b=1}^{3} \frac{1}{\lambda_b}\frac{\partial S_a}{\partial \lambda_b}\hat{N}_a \otimes \hat{N}_a \otimes \hat{N}_b \otimes \hat{N}_b + \sum_{a,b=1,a\neq b}^{3} \frac{S_b - S_a}{\lambda_b^2 - \lambda_a^2}(\hat{N}_a \otimes \hat{N}_b \otimes \hat{N}_a \otimes \hat{N}_b + \hat{N}_a \otimes \hat{N}_b \otimes \hat{N}_b \otimes \hat{N}_a) \quad (19)$$

Finally, we perform an iterative optimization to determine the Young's modulus and Poisson's ratio fields that optimally approximate the components this tensor. This Young's modulus is what we ultimately report as the lung's stiffness (Fig. 1(d)).

2.5 Statistical comparison of intergroup and intragroup strains and stiffnesses

To characterize changes in strain and stress fields with pressure, we discretized the domain by coherence length into 50x50 pixel patches (See Fig. S5), the dimensions of which were chosen to minimize the correlation between image patches. We then computed the mean within each patch, along with the standard deviation across patches within the same domain. With these means and standard deviations, P-values were computed (i) across image patches within the same field in order to examine the significance of spatial variations in strain and stiffness and (ii) across pressures within the same patch in order to examine the significance of pressure-driven changes in strain and stiffness within a given patch.

3 Results and discussion

3.1 Validating the finite-element model

We begin by describing and assessing the finite-element model of the organ, which constitutes the first stage of the system. The image classifiers described in the methods yield high-quality segmentations of the lung and the ribcage. These segmentations are subsequently used to construct a realistic, though simplified, model of the lung within the crystal ribcage (Fig. 2(a)). We find that the pressure-stretch curve of the finite-element model changes smoothly with the parameter α of the hyperelastic foam model; from these curves, we construct a smooth surface approximating the transpulmonary pressure as a function of stretch λ and material parameter α (Fig. 2(b)). Having characterized how the finite-element model's response changes with α, we solve for the values of μ and α that maximize the likelihood of observing the distensions that we measure in the crystal ribcage; for the data collected in the present study, we determine that the optimal value for μ is 0.61 kPa and for α is 12.4 (Fig. 2(c)) through the optimization described earlier. The general form of the hyperelastic foam model consists of multiple additive terms. Although a greater number of terms should in theory lead to a better approximation of the data, fitting a model with multiple

terms is complicated by the model's nonlinearity in the α parameter, so that it is not possible to reuse the calibration surface to fit successive terms beyond the first. For simplicity and because the subsequent outcome is adequate for our purposes, we settle for a single term. We observe that the qualitative distension of the finite-element model matches that of the real lung in the crystal ribcage (Fig. 2(d)). Despite the finite-element model's homogeneous material properties, its strains (Fig. 2(e)) and stresses (Fig. 2(f)) grow increasingly heterogeneous across the lung's surface as the pressure increases, with the highest values occurring near the spine.

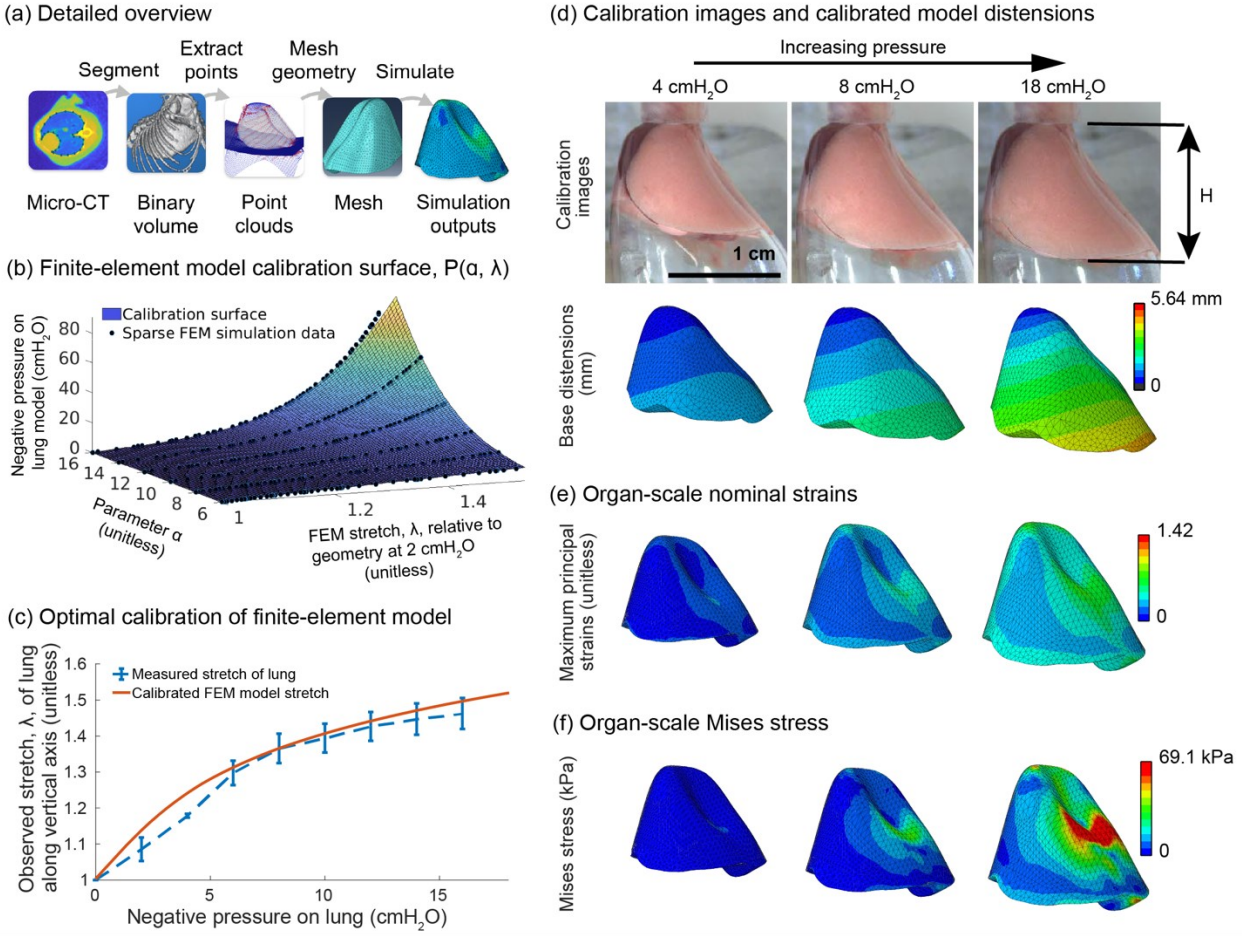

Figure 2 | Constructing the finite-element model of the lung from a microCT volume and organ-scale pressure-distension data. (a) A Bayesian classifier segments the mouse lung and ribcage from a microCT volume[44-46] of the mouse thorax. From the segmentations, we construct smooth point clouds approximating the interior surfaces of the ribcage and of the diaphragm. From these point clouds, we construct solid models in SolidWorks and then mesh those models in Abaqus. (b) Pressure versus vertical stretch, λ, is recorded for simulations across a range of values for the material parameter α. Because the model is linear in the material parameter μ, this allows us to produce a predictive model of transpulmonary pressure versus distension for a wide range of material coefficients based on a limited number of forward simulations. The parameter α controls the nonlinearity of the model. The parameter μ controls the initial slope of the model in the small-strain regime. Having characterized the model in (b), we can solve (c) for the optimal material coefficients from stereomicroscope images of the lung in the crystal ribcage shown in (d). (e, f) Strains and stresses in the lung throughout the finite-element model.

3.2 Validating the multiscale model

After constructing the finite-element model and calibrating its material constants, we proceed to evaluate the system's predictive performance. To do so, we modify the calibrated finite-element model to contain a stiffer inclusion representing a tumor (Fig. 3(a)). From the displacements of this model over a range of pressures, we solve the inverse elasticity problem in the vicinity of the tumor. Across the entire range of distending pressures, we find that the total areal strain (Fig. 3(b)) is highly correlated with the ground-truth stiffness (Fig. 3(c)). We further find that the stiffness estimate produced by our multiscale model (Fig. 3(d)) is well-correlated with the ground truth. Although the prediction is somewhat biased relative to the ground truth, we find that the mean of the predicted stiffness is strongly correlated with the mean of the ground truth both inside and outside the tumor (Fig. 3(e)). In a simpler setting, preliminary studies also indicate that the nonlinear formulation of the inverse elasticity problem accurately predicts the stiffness distribution throughout a 2D, hyperelastic membrane (Fig. S4). In contrast, preliminary studies also indicate that a piecewise-linear formulation of the inverse elasticity problem fails to do so (Fig. S5).

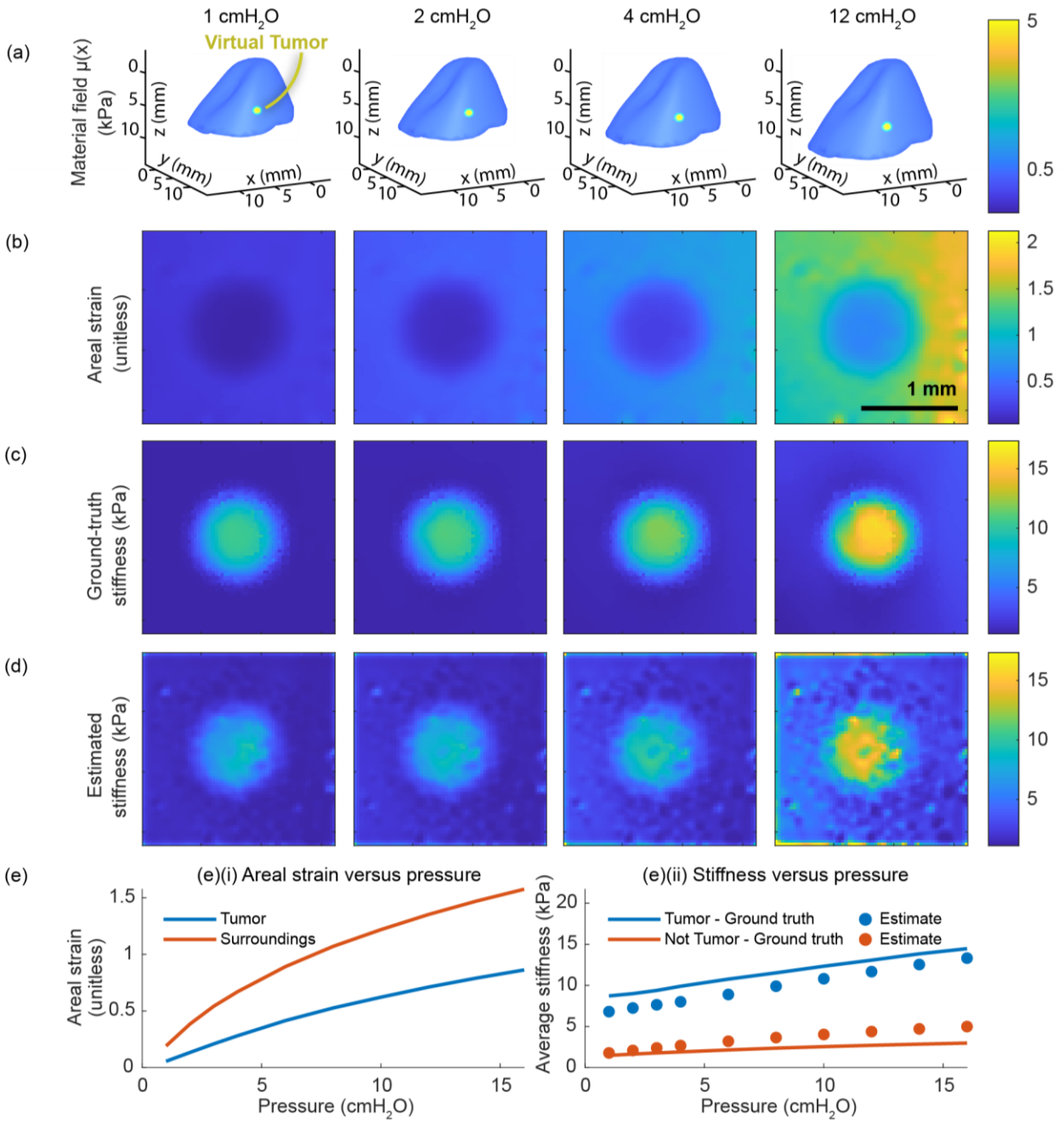

Figure 3 | End-to-end validation of the whole-organ and microscale models. The validation includes applying the multiscale model to a finite-element model whose material field contains an inclusion representing a cancerous tumor. (a) The material field superposed over the deformed geometry of the finite-element model across a range of distending pressures. (b) The total areal strain at a subset of these same pressures. (c) The ground-truth stiffness distribution throughout the finite-element model determined from material field, the hyperelastic constitutive equation, and the state of deformation. (d) The corresponding stiffnesses in absolute units (kPa) throughout the domain determined by our model based on the simulated displacements. (e) The cumulative areal strain and the absolute stiffness change nonlinearly with the distending pressure. (e)(i) The average, nominal areal strain inside the tumor is consistently lower than the same outside the tumor. (e)(ii) The mean value of the ground-truth stiffness distribution is strongly correlated with the stiffness distribution predicted by the multiscale model.

3.3 Lung stiffness at alveolar resolution

After validating the model, we next apply the model to real images of the lung in the crystal ribcage to measure the stiffness of the lung in absolute units and at alveolar resolution. First, we apply the model to images of the same region of interest in the healthy lung over a range of distending pressures (Fig. 4(a)). To demonstrate the accuracy of the registration, we warp them back to the reference configuration at 2 cmH_2O (Fig. 4(b)). We observe that the areal strain varies substantially on the length scale of an individual alveolus, with airspaces stretching much more than the septum (Fig. 4(c)). Likewise, we see that the stiffness varies on a similar length scale, and we report for the first time, a noninvasive measurement of the absolute stiffness of the lung's surface both in the airspace and in the septum; stiffnesses within the airspace are close to 1-2 kPa, while stiffnesses in the septum commonly reach as high as 15 kPa at higher pressures (Fig. 4(d)). These values are consistent with measurements taken using other techniques like atomic-force microscopy (AFM), for which estimates for the lung's shear modulus commonly range from 0.5 to 3 kPa.[65,66] Another study[67] predicted that the Young's modulus of the septum ranges from 12 kPa at low transpulmonary pressures to 140 kPa at high transpulmonary pressures; the lower bound is very close to our estimate, while the upper bound is of the same magnitude as ours (Fig. 4(d)). Perhaps most significantly, we observe that the pattern of stiffnesses throughout the domain is conserved across the entire range of pressures. Finally, we note that the mean stiffness of the tissue rises linearly up to 7 cmH_2O, and then the stiffness quickly plateaus with increasing transpulmonary pressure (Fig. 4(e-f)). Based on the scheme previously described in the methods (Fig. S6), P-values computed using Student's t-test indicate that the change in strain across pressures is statistically significant with $p < 0.05$ from 5-7 cmH_2O, 7-12 cmH2O, and 12-18 cmH2O (Fig. 4(f)). On the other hand, the change in stiffness is only statistically significant at lower pressures, owing to higher variance in the stiffness and its apparent plateau at higher pressures. We also predict that the variance in the lung's stiffness increases with distension (Fig. 4(f)); this prediction is consistent with our previous, independent measurement of the lung's strain-stiffening behavior from manual measurements of alveolar areas across different pressures.[36] To our knowledge, this is the first time that the lung's stiffness, and its change with distension, has been measured under *ex vivo* conditions with physiologically realistic boundary conditions in absolute units and at alveolar resolution.

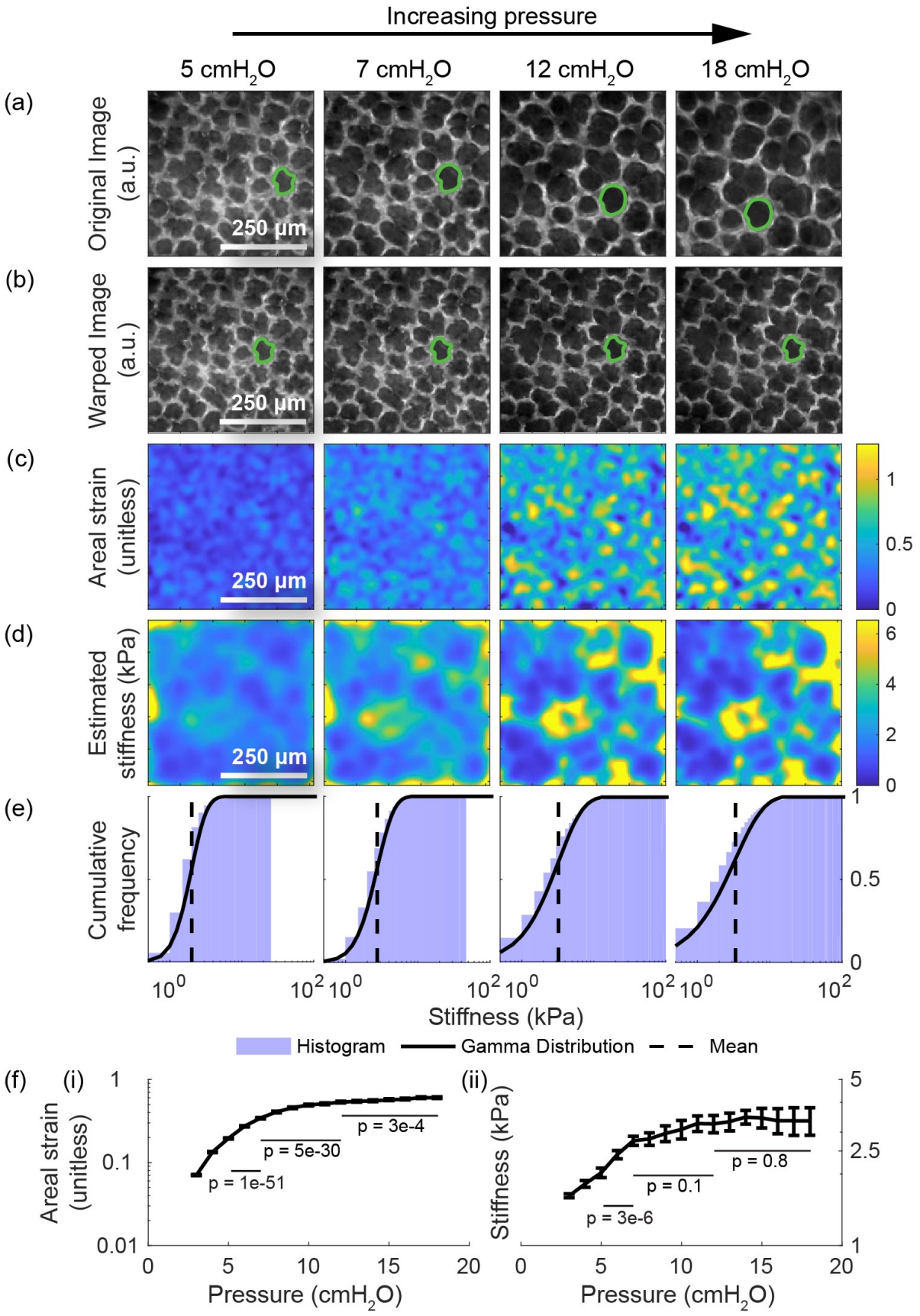
Increasing pressure
5 cmH2O
7 cmH2O
12 cmH2O
18 cmH2O
(a)
Original Image (a.u.)
250 μm
(b)
Warped Image (a.u.)
250 μm
(c)
Areal strain (unitless)
250 μm
1
0.5
0
(d)
Estimated stiffness (kPa)
250 μm
6
4
2
0
(e)
Cumulative frequency
1
0.5
0
10^0
10^2
Stiffness (kPa)
Histogram
Gamma Distribution
Mean
(f)
(i)
Areal strain (unitless)
1
0.1
0.01
p = 1e-51
p = 5e-30
p = 3e-4
0
5
10
15
20
Pressure (cmH2O)
(ii)
Stiffness (kPa)
5
2.5
1
p = 3e-6
p = 0.1
p = 0.8
Pressure (cmH2O)

Figure 4 | Providing the alveolus-scale stiffness map during the full breathing cycle in the healthy lung. (a) The same region of interest within a healthy lung from a transgenic, mTmG mouse expressing the tdTomato fluorescent label at four different distending pressures. (b) The result of computationally deforming these images back to the lung's geometry at 2 cmH_2O using the registered displacements. The displacement maps used to deform these images were subsequently used as inputs to the multiscale model to determine the distribution of stiffnesses throughout the healthy tissue. (c) The areal strain relative to the geometry at 2 cmH_2O. We observe that the qualitative pattern in the computed strains is largely conserved across all pressures. Row (d) depicts the corresponding stiffnesses in absolute units throughout the domain determined by applying our model to these images. As with the areal strain maps, the stiffness maps are qualitatively similar across the whole range of pressures. (e) The histogram and corresponding Gamma distribution of the stiffnesses throughout the domain, demonstrating that the mean and the heterogeneity in the lung's stiffness increase with distension. (f) The nonlinear change in mean strain and mean stiffness with the distending pressure. The error bars represent the standard error from the mean, computed by discretizing the domain into a coherence length of 50x50 pixel patches (See Fig. S6). Computed using Student's t-test, P-values are shown for the change in strain (and for the change in stiffness) from 5-7 cmH_2O, 7-12 cmH_2O, and 12-18 cmH_2O; the strains are consistently statistically significant, while the stiffnesses are begin statistically significant and then decrease in significance. We further observe that the variance in the stiffness increases with transpulmonary pressure, which is consistent with our previous finding on relative stiffness.[36]

Having applied the model to the healthy lung, we do the same for images of the lung with cancer (Fig. 5(a)) to characterize the effect of cancer on the lung's material properties. As with the previous figure, the second row (Fig. 5(b)) shows the result of deforming these images back to the geometry of the lung at 2 cmH_2O using the registered displacements. Here, we observe that the strain inside the tumor is substantially lower than the strain outside the tumor across all measured pressures (Fig. 5(c)). Consistent with these observations, the estimated stiffness inside the tumor is substantially higher than the stiffness outside at lower pressures (Fig. 5(d)). Whereas the majority of stiffnesses in the healthy lung are below 5 kPa at pressures up to 10 cmH_2O, a large fraction of the tumor exceeds these stiffnesses at these same pressures (Fig. 5(f)). Using the method described previously (Fig. S6), P-values computed using Student's t-test indicate that the change in strain across pressures within the lung tissue is statistically significant with $p < 0.05$ from 5-7 cmH_2O, 7-12 cmH2O, and 12-18 cmH2O, while changes in the strain within the tumor are insignificant at 7-12 cmH2O and 12-18 cmH2O (Fig. 5(f)). Once again, in both types of tissue, the change in stiffness decays in significance with increasing pressure. On the other hand, at the same pressure, the difference in strain and stiffness across groups (i.e. lung or tumor) is statistically significant with $p < 0.05$ across all pressures.

Relative to the healthy case, we also observe that the stiffness of the tissue outside the tumor is depressed by about 20%, suggesting that the tumor may remodel the lung even in regions that are not visible by light microscopy alone; whether that remodeling is due to the tumor visible in the images or due to other tumors that are below the lung's surface is not clear. Moreover, while the mean stiffness of the lung tissue increases in nonlinear fashion as in the case of the healthy lung, the mean stiffness of the tumor increases much more quickly (Fig. 5(e)). In summary, this measurement represents the first measurement of the absolute stiffness of a lung tumor under physiologically realistic boundary conditions and at alveolar resolution, and we see evidence of remodeling beyond the visible bounds of the tumor. Supplemental figures (Fig. S7-S9) depict these same maps across the entire range of transpulmonary pressures.

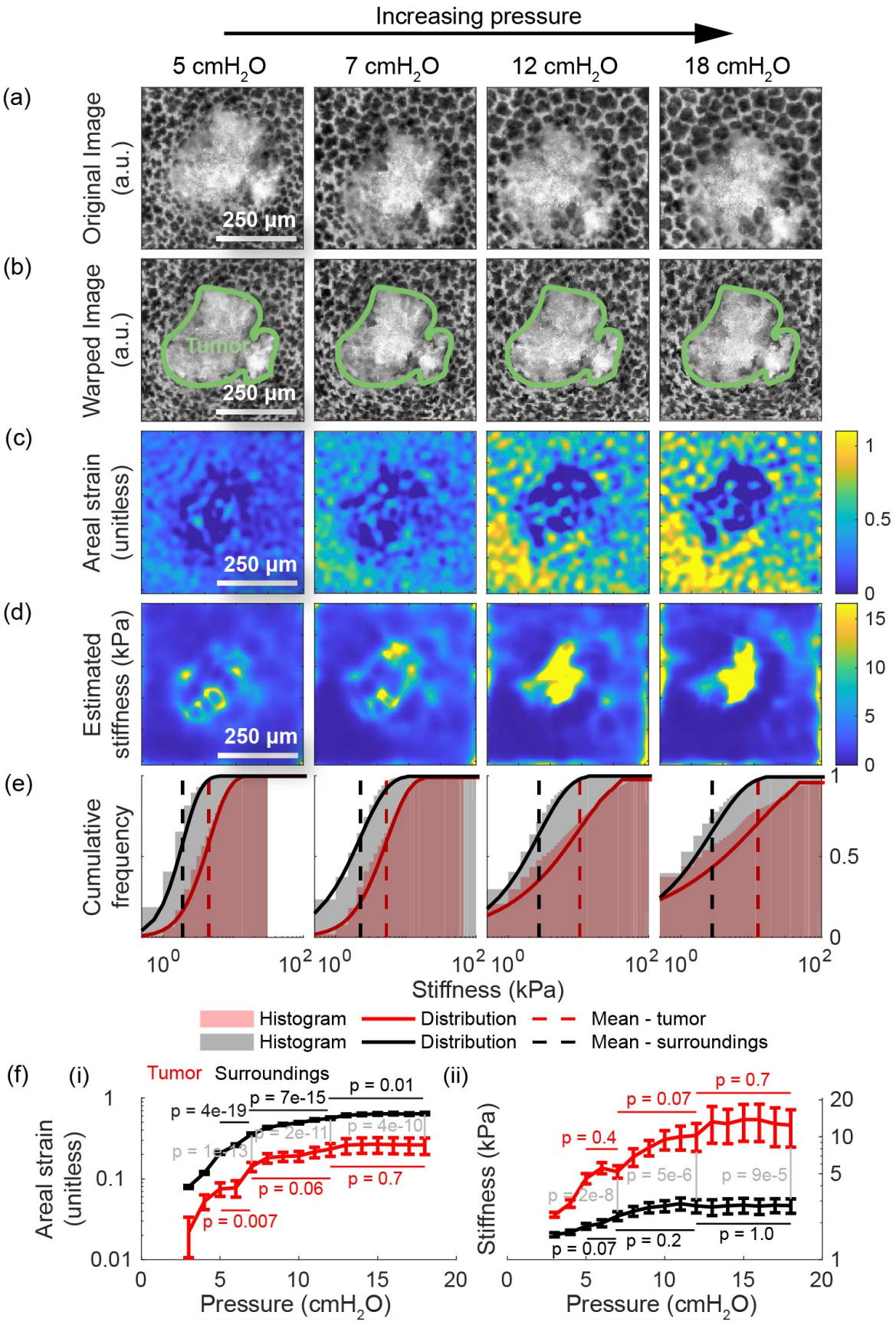
Increasing pressure
5 cmH2O
7 cmH2O
12 cmH2O
18 cmH2O
(a)
Original Image (a.u.)
250 μm
(b)
Warped Image (a.u.)
Tumor
250 μm
(c)
Areal strain (unitless)
250 μm
1
0.5
0
(d)
Estimated stiffness (kPa)
250 μm
15
10
5
0
(e)
Cumulative frequency
1
0.5
0
10^0
10^2 10^0
10^2 10^0
10^2 10^0
10^2
Stiffness (kPa)
Histogram
Distribution
Mean - tumor
Histogram
Distribution
Mean - surroundings
(f)
(i)
Tumor
Surroundings
Areal strain (unitless)
1
0.1
0.01
p = 4e-19
p = 7e-15
p = 0.01
p = 2e-11
p = 4e-10
p = 1e-13
p = 0.06
p = 0.7
p = 0.007
0
5
10
15
20
Pressure (cmH2O)
(ii)
Stiffness (kPa)
20
10
5
1
p = 0.07
p = 0.7
p = 0.4
p = 5e-6
p = 9e-5
p = 2e-8
p = 0.07
p = 0.2
p = 1.0
0
5
10
15
20
Pressure (cmH2O)

Figure 5 | Applying the model to the lung with cancer. (a) The same region of interest within a lung presenting with primary cancer from a transgenic, mTmG mouse expressing the tdTomato fluorescent label at four different distending pressures. These images were used as inputs to the multiscale model to determine the distribution of stiffnesses throughout the tumor and its surroundings. (b) The result of computationally deforming these images back to the geometry at 2 cmH_2O using the registered displacements. (c) The corresponding areal strain, relative to the geometry at 2 cmH_2O, induced by the given increase in transpulmonary pressure. As with healthy tissue, the range of areal strains decreases with increasing transpulmonary pressure, indicating an increase in tissue stiffness. Unlike healthy tissue, the tumor clearly exhibits much lower stretch than the surroundings. (d) The corresponding stiffnesses in absolute units throughout the domain determined by applying our model to these images. At lower pressures, the tumor is significantly stiffer than its surroundings. The intratumor and extratumor stiffnesses both increase with transpulmonary pressure. (e) The stiffness distributions show that the tumor is consistently stiffer surrounding tissue across all pressures, with tumors having higher maximum stiffness and greater variability in stiffness. (f) Compared to surrounding tissue, the tumor deforms less with increasing transpulmonary pressure ((f)(i)); stiffens more ((f)(ii)), notably being 4.8 times stiffer at 18 cmH_2O; and exhibits greater variance in stiffness, mirroring trends seen in earlier figures. Computed using Student's t-test, P-values are shown for the change in strain (and for the change in stiffness) from 5-7 cmH_2O, 7-12 cmH_2O, and 12-18 cmH_2O. Additionally, P-values are shown comparing the strain and stiffness of the lung tissue versus the tumor tissue at pressures 7 cmH_2O, 12 cmH_2O, and 18 cmH_2O; the differences between classes are statistically significant for all pressure changes.

3.4 A hypothesis explaining the experimental data

To explain the preceding observations, we briefly reflect on the biochemical structures and physical principles that determine the material properties of the lung and solid tumors. The primary load-bearing elements of the extracellular matrix are elastin, collagen type-1, and collage type-3.[56] Although two isolated collagen helices with the same geometric configuration should exhibit identical material properties, determined by the interplay between intramolecular and intermolecular forces between monomeric subunits of the triple helix[68], it is well-known that collagen arranges itself into more complex, hierarchical structures.[69] Within these structures, greater cross-linking between individual collagen helices increases the stiffness at the tissue scale.[69] Furthermore, given that entropic effects largely dominate in determining the material properties of rubber-like polymer networks, the current geometric configuration of a polymer network influences its current stiffness.[70-74] Finally, recalling that networks of parallel springs are stiffer than networks of springs in series,[68] we observe that the stiffness of such a network largely depends on its topology. Variations in any of these three contributors can therefore lead to variations in tissue stiffness at cellular, alveolar, and organ length scales.

Based on the biochemical structure of the extracellular matrix, there are thus four obvious reasons why the tumor should be stiffer than the surrounding tissue. First, unlike the healthy lung which contains airspaces, solid tumors are generally aggregates of cells and extracellular matrix lacking holes or gaps at the cellular length scale; their simply connected structure therefore elevates their stiffness relative to the multiply connected structure of the healthy parenchyma. Second, even if we ignore the airspaces, pathologically elevated deposition of extracellular matrix within the tumor increases the matrix's density compared to healthy tissue, and greater density is naturally associated with elevated stiffness essentially because there are more load-bearing elements at the molecular level.[1] Third, pathologically elevated cross-linking also increases the stiffness of the extracellular matrix. Fourth, while the polyhedral topology of the parenchyma essentially forces the alignment of collagen fibrils within the mid-plane of the septum and reduces the entropy of the extracellular matrix, the collagen fibrils within solid tumors can be arranged in arbitrary orientations; stretching a solid tumor by the same distance should therefore affect the quantity of work required to produce the same stretch.

Next, we discuss the physical source of strain stiffening. First, we note that statistical thermodynamics predicts that single polymer molecules exhibit strain-stiffening behavior; as the molecule stretches, the number of available geometric configurations decreases, the change in entropy between successive states of elongation increases, and thus the force required to produce the same distension monotonically increases with stretch.[71,72,74,75] Indeed, recent Steered Molecular Dynamics simulations of individual collagen helices predicted that these polymers exhibit strain-stiffening, with their stiffnesses ranging from 5 kPa to 15 kPa.[68] At higher levels of organization, AFM studies confirm that individual collagen fibrils also grow stiffer with strain[76,77], and that collagen-based biomaterials likewise exhibit the same behavior.[69,77] Most likely, then, the strain-stiffening behavior at the tissue scale directly follows from the strain-stiffening behavior of individual collagen helices at the molecular scale. This is, essentially, the central hypothesis underpinning classical derivations of constitutive equations for hyperelastic materials, and it motivates our choice of a hyperelastic material law.[55,70]

The theory of percolation[78], which predicts that stretch produces gradual straightening and alignment of initially wave collagen fibers, may seem to imply that the lung's stiffness should grow increasingly homogeneous with increasing stretch. But our observation that stiffness heterogeneity increases with pressure, an effect referred to as heteroscedasticity in the statistics literature[50], directly contradicts this hypothesis. Several studies agree with our prediction across multiple length scales. First, studies on the strain-stiffening behavior of individual collagen fibrils have also reported that the variance in fibril stiffness increases with strain[76,77]. Second, at the alveolar length scale, both spring-network studies[79,80] and finite-element analysis studies[81] have consistently predicted an increase in septal stiffness heterogeneity with pressure. Finally, at the organ scale, registration-based studies[82,83] have reported the same. However, one recent multiscale, AFM study[65] measured heteroscedasticity in macroscopic slices of decellularized lung tissue, but that same study did not observe the same trend for microscopic slices. One possible explanation for this disagreement is that tissue resection disrupts this phenomenon. Another possible explanation is that our method computes the variance over the stiffness both in the airspace and in the septum, but that does not explain why the aforementioned studies have reported the same phenomenon. Although we cannot discount that the geometric configuration of the individual polymers within the network somehow contributes to this behavior, the heteroscedasticity at the tissue scale may arise, at least in part, from the heteroscedasticity of the individual collagen fibrils comprising the extracellular matrix.

3.5 Addressing assumptions in our model

Although these findings represent a significant advance in our ability to quantify the lung's mechanical properties at cellular resolution in both health and disease, the model makes several simplifying assumptions that we should acknowledge. These assumptions, which vary in the magnitude of their potential impacts, include (i) approximating the Jacobian as $(\lambda_1\lambda_2)^{1.5}$ when solving the inverse elasticity problem, (ii) adopting the same constitutive equation at the alveolar and organ length scales, (iii) assuming that the Poisson ratio is 0.2 at both length scales, (iv) neglecting higher-order features of the lung, such as interlobular fissures and airways, when constructing the finite-element model's geometry, (v) assuming that the lung's stiffness is generally homogeneous at the organ scale, (vi) treating the airspace as a tensile element when

solving the inverse problem, (vii) assuming isotropicity when solving for the Young's modulus, and (viii) neglecting the influence of gravity on the lung's deformation.

In Fig. S8, assumption (i) was shown to exert a relatively minor effect, typically introducing less than 10% error into our approximation of the Jacobian determinant. To address assumption (ii), we observe that the extracellular matrix is the primary determinant of the lung's material properties across all length scales. While studies have shown that the lung's macroscale stiffness is significantly less than the stiffness of individual lung cells[84], owing to the porosity of the tissue, our approach ensures that the average stiffness, computed across many alveoli over both the airspace and the septum, matches the organ-scale stiffness. As the number of alveoli in the calculation approach the total number of alveoli in the lung, this average must approach the whole lung's average stiffness. Consequently, we argue it is reasonable to enforce equality between these quantities. This same reasoning also justifies assumption (iii).

Assumption (iv) is, in part, justified on the basis that parenchyma comprises over 95% of the lung's total volume[85], which implies that the effect of stiffer airways on the deformation should be small in the distal parts of the lung. On the other hand, evidence suggests[86] that the interlobular fissures relieve stress that may develop on the surface of the lung in their absence. This assumption, therefore, may affect the accuracy depending on the proximity to a fissure.

Assumption (v) is challenged by MRE studies[87] that reveal significant regional variation in lung compliance at the organ scale. For healthy individuals, this study reported that the mean shear modulus was 0.849 ± 0.250 kPa at residual volume and 1.33 ± 0.195 kPa at total lung capacity. Consequently, the standard deviation decreases from about 30% of the mean value at residual volume to about 15% of the mean at total lung capacity. Consequently, we may expect our stiffness maps to incur similar errors due to this assumption. Because our images are collected within microns of the pleural surface, we suspect that the airspace region in the images effectively exhibits some resistance to deformation, justifying assumption (vi); even if the airspace lacks effective stiffness, that should be reflected by a low value in the stiffness mapping, which is exactly what is shown in Fig. 4 and Fig. 5. Finally, in support of assumption (vii), we performed simulations of the finite-element model with an embedded inclusion, and we found that assuming isotropicity (Fig. S10) led to similar results as assuming orthotropicity (Fig. S11), with both models in reasonable agreement with the ground truth (Fig. S12).

Assumption (viii), the decision to neglect gravity in modeling the lung, was addressed previously in the methods. Briefly, although previous studies[56,57] have shown that gravity significantly influences the mechanics of the human lung, similar studies have not been done in the mouse. We offer two arguments, however, in support of our position. First, these previous studies on the human lung suggest that gravity is insignificant to the solid mechanics of the mouse lung. One recent theoretical analysis[56] on the human lung distilled the influence of gravity on alveolar mechanics to the weight of tissue below a given alveolus; consequently, the study found that the effects of gravity are more significant near the apex than the base. Because the weight of the mouse lung is about 1 gram, and because the stiffness of the mouse lung is similar to that of the human lung, its weight according to this model should not significantly influence its mechanical behavior. Using CT images to measure regional variations in lung density, another study[57] showed that gravity causes the density of the human lung to increase linearly with vertical displacements

toward the Earth; critically, the study showed that lung density only changes by a few percent of the mean with displacements near 1 cm. Because the density and stiffness of the mouse lung is similar to that of the human lung, we likewise expect gravity to have only a modest influence on tissue density in the mouse. Second, as described earlier in the methods, dimensional analysis[58] reveals that the stresses developed within the mouse lung are significantly larger than the hydrostatic stresses arising due to gravity.

4 Conclusion

We have built the first model capable of measuring the absolute stiffness of the lung at microscale resolution and under physiologically realistic boundary conditions. We have shown that our model can measure the nonlinear stiffening of the lung with increasing stretch, and that the relative stiffness distribution throughout the domain is, at least in the case of the healthy lung, largely conserved across a range of pressures, giving further confidence that our prediction corresponds to reality since these stiffness maps have been produced by completely different displacement maps. Furthermore, we have shown that our model's quantitative predictions are consistent with state-of-the-art measurements based on AFM. Finally, we have demonstrated the capability of our model to identify and measure the stiffness of tumors within the lung tissue. Here, we have shown, for the first time, that the tumor exhibits similar strain-stiffening behavior to the lung tissue itself, but that the tumor stiffens more substantially than the surroundings; in the state of greatest distension, for example, the tumor's mean stiffness is 4.8 times greater than that of the surroundings. Additionally, because the variance in the stiffness increases with transpulmonary pressure, we have shown that the heterogeneity in the stiffness distribution likewise increases with pressure, with greater heterogeneity in the tumor than in the surroundings.

Author Contributions

RL jointly conceived the approach, built the model, validated the model, applied the model, analysed the results, and wrote the manuscript. HTN jointly conceived the approach and wrote the manuscript. GG collected high-resolution microscopy images of the lung in health and disease, along with low-resolution stereomicroscope images of the lung for calibrating the organ-scale model, and contributed to the manuscript's empirical methods. RB built the crystal ribcage platform and described its construction in the methods. KR collaborated on the development of the inverse solver and edited the manuscript. BS provided valuable feedback and edited the manuscript.

Acknowledgements

A. Coats from the Hoffman laboratory at the University of Iowa provided the microCT image datasets used to fabricate the crystal ribcage. Any opinion, findings and conclusions or recommendations expressed in this material are those of the authors and do not necessarily reflect the views of the National Science Foundation. H.T.N. discloses support for the research described in this study from the National Institutes of Health R21EB031332 and DP2HL168562, a Beckman Young Investigator Award, an NSF CAREER Award, Kilachand Fund, Boston University Center for Multiscale and Translational Mechanobiology and a Dean's Catalyst Award and the American Cancer Society Institutional Fund at Boston University. This material is also based upon work supported by the National Science Foundation and G.N.G. acknowledges support from the NSF Graduate Research Fellowship, grant no. 2234657. The funders had no role in study design, data

collection and analysis, decision to publish or preparation of the manuscript. We also thank P. Barbone for his valuable guidance on developing the inverse-elasticity software.

References

1 Nia, H. T., Munn, L. L. & Jain, R. K. Physical traits of cancer. *Science* **370**, eaaz0868 (2020). https://doi.org:doi:10.1126/science.aaz0868

2 Zhang, S. *et al.* The peritumor microenvironment: physics and immunity. *Trends in Cancer* **9**, 609-623 (2023). https://doi.org:10.1016/j.trecan.2023.04.004

3 Ulrich, T. A., De Juan Pardo, E. M. & Kumar, S. The Mechanical Rigidity of the Extracellular Matrix Regulates the Structure, Motility, and Proliferation of Glioma Cells. *Cancer Research* **69**, 4167-4174 (2009). https://doi.org:10.1158/0008-5472.can-08-4859

4 Tse, J. M. *et al.* Mechanical compression drives cancer cells toward invasive phenotype. *Proceedings of the National Academy of Sciences* **109**, 911-916 (2012). https://doi.org:10.1073/pnas.1118910109

5 Wirtz, D., Konstantopoulos, K. & Searson, P. C. The physics of cancer: the role of physical interactions and mechanical forces in metastasis. *Nature Reviews Cancer* **11**, 512-522 (2011). https://doi.org:10.1038/nrc3080

6 Boyd, N. F. *et al.* Evidence That Breast Tissue Stiffness Is Associated with Risk of Breast Cancer. *PLoS ONE* **9**, e100937 (2014). https://doi.org:10.1371/journal.pone.0100937

7 Evans, A. *et al.* Differentiating benign from malignant solid breast masses: value of shear wave elastography according to lesion stiffness combined with greyscale ultrasound according to BI-RADS classification. *British Journal of Cancer* **107**, 224-229 (2012). https://doi.org:10.1038/bjc.2012.253

8 Cochlin, D., Ganatra, R. H. & Griffiths, D. F. R. Elastography in the Detection of Prostatic Cancer. *Clinical radiology.* **57**, 1014-1020 (2002). https://doi.org:10.1053/crad.2002.0989

9 Goenezen, S. *et al.* Linear and Nonlinear Elastic Modulus Imaging: An Application to Breast Cancer Diagnosis. *IEEE Transactions on Medical Imaging* **31**, 1628-1637 (2012). https://doi.org:10.1109/tmi.2012.2201497

10 Panzetta, V. *et al.* Mechanical phenotyping of cells and extracellular matrix as grade and stage markers of lung tumor tissues. *Acta Biomaterialia* **57**, 334-341 (2017). https://doi.org:10.1016/j.actbio.2017.05.002

11 Nia, H. T., Munn, L. L. & Jain, R. K. Mapping Physical Tumor Microenvironment and Drug Delivery. *Clinical Cancer Research* **25**, 2024-2026 (2019). https://doi.org:10.1158/1078-0432.ccr-18-3724

12 Nia, H. T. *et al.* In vivo compression and imaging in mouse brain to measure the effects of solid stress. *Nature Protocols* **15**, 2321-2340 (2020). https://doi.org:10.1038/s41596-020-0328-2

13 Nia, H. T. *et al.* Quantifying solid stress and elastic energy from excised or in situ tumors. *Nature Protocols* **13**, 1091-1105 (2018). https://doi.org:10.1038/nprot.2018.020

14 Nia, H. T. *et al.* Solid stress and elastic energy as measures of tumour mechanopathology. *Nature Biomedical Engineering* **1**, 0004 (2016). https://doi.org:10.1038/s41551-016-0004

15 Zhang, S. *et al.* Intravital measurements of solid stresses in tumours reveal length-scale and microenvironmentally dependent force transmission. *Nature Biomedical Engineering* **7**, 1473-1492 (2023). https://doi.org:10.1038/s41551-023-01080-8

16 Seidl, D. T., Van Bloemen Waanders, B. G. & Wildey, T. M. Simultaneous inversion of shear modulus and traction boundary conditions in biomechanical imaging. *Inverse Problems in Science and Engineering* **28**, 256-276 (2020). https://doi.org:10.1080/17415977.2019.1603222

17 Ghiuchici, A.-M. *et al.* Is There a Place for Elastography in the Diagnosis of Hepatocellular Carcinoma? *Journal of Clinical Medicine* **10**, 1710 (2021). https://doi.org:10.3390/jcm10081710

18 De, S., Guilak, F., Mofrad R K, M., Barbone, P. E. & Oberai, A. A. A Review of the Mathematical and Computational Foundations of Biomechanical Imaging. *Computational Modeling in Biomechanics*, 375-408 (2010). https://doi.org:info:doi/10.1007/978-90-481-3575-2_13

19 Costa, K. D. Single-Cell Elastography: Probing for Disease with the Atomic Force Microscope. *Disease Markers* **19**, 139-154 (2004). https://doi.org:10.1155/2004/482680

20 Garra, B. S. Elastography: history, principles, and technique comparison. *Abdominal Imaging* **40**, 680-697 (2015). https://doi.org:10.1007/s00261-014-0305-8

21 Kennedy, B. F., Kennedy, K. M. & Sampson, D. D. A Review of Optical Coherence Elastography: Fundamentals, Techniques and Prospects. *IEEE journal of selected topics in quantum electronics : a publication of the IEEE Lasers and Electro-optics Society.* **20**, 272-288 (2014). https://doi.org:10.1109/JSTQE.2013.2291445

22 Kuo, Y.-W. *et al.* Application of transthoracic shear-wave ultrasound elastography in lung lesions. *European Respiratory Journal* **57**, 2002347 (2021). https://doi.org:10.1183/13993003.02347-2020

23 Schregel, K. *et al.* Characterization of glioblastoma in an orthotopic mouse model with magnetic resonance elastography. *NMR in Biomedicine* **31**, e3840 (2018). https://doi.org:10.1002/nbm.3840

24 Silva, L. D. C. M. D. *et al.* Ultrasound elastography in patients with fatty liver disease. *Radiologia Brasileira* **53**, 47-55 (2020). https://doi.org:10.1590/0100-3984.2019.0028

25 Wang, C. *et al.* Optical coherence elastography and its applications for the biomechanical characterization of tissues. *Journal of Biophotonics* **16** (2023/12/01). https://doi.org:10.1002/jbio.202300292

26 Krieg, M. *et al.* Atomic force microscopy-based mechanobiology. *Nature Reviews Physics* **1**, 41-57 (2018). https://doi.org:10.1038/s42254-018-0001-7

27 Liu, F. & Tschumperlin, D. J. Micro-Mechanical Characterization of Lung Tissue Using Atomic Force Microscopy. *Journal of Visualized Experiments* (2011). https://doi.org:10.3791/2911

28 Barbone, P. E. & Gokhale, N. H. Elastic modulus imaging: on the uniqueness and nonuniqueness of the elastography inverse problem in two dimensions. *Inverse problems* **20**, 283 (2004).

29 Barbone, P. E. & Bamber, J. C. Quantitative elasticity imaging: what can and cannot be inferred from strain images. *Physics in Medicine & Biology* **47**, 2147 (2002).

30 Cercos-Pita, J.-L. *et al.* Lung tissue biomechanics imaged with synchrotron phase contrast microtomography in live rats. *Scientific Reports* **12** (2022). https://doi.org:10.1038/s41598-022-09052-9

31 Kennedy, B. F., Wijesinghe, P. & Sampson, D. D. The emergence of optical elastography in biomedicine. *Nature Photonics* **11**, 215-221 (2017). https://doi.org:10.1038/nphoton.2017.6

32 Nelson, T. M. *et al.* Diseased and healthy murine local lung strains evaluated using digital image correlation. *Scientific Reports 2023 13:1* **13** (2023-03-20). https://doi.org:10.1038/s41598-023-31345-w

33 Maghsoudi-Ganjeh, M., Mariano, C. A., Sattari, S., Arora, H. & Eskandari, M. Developing a Lung Model in the Age of COVID-19: A Digital Image Correlation and Inverse Finite Element Analysis Framework. *Frontiers in Bioengineering and Biotechnology* **9** (2021). https://doi.org:10.3389/fbioe.2021.684778

34 Regan, K. *et al.* Multiscale elasticity mapping of biological samples in 3D at optical resolution. *Acta biomaterialia.* (2023). https://doi.org:10.1016/j.actbio.2023.12.036

35 Kim, J. H. *et al.* Multiscale stiffness of human emphysematous precision cut lung slices. *Science Advances* **9** (2023). https://doi.org:10.1126/sciadv.adf2535

36 Banerji, R. *et al.* Crystal ribcage: a platform for probing real-time lung function at cellular resolution. *Nature Methods* (2023). https://doi.org:10.1038/s41592-023-02004-9

37 Looney, M. R. & Bhattacharya, J. Live Imaging of the Lung. *Annual Review of Physiology* **76**, 431-445 (2014). https://doi.org:10.1146/annurev-physiol-021113-170331

38 Looney, M. R. *et al.* Stabilized imaging of immune surveillance in the mouse lung. *Nature Methods* **8**, 91-96 (2011). https://doi.org:10.1038/nmeth.1543

39 Entenberg, D. *et al.* A permanent window for the murine lung enables high-resolution imaging of cancer metastasis. *Nature Methods* **15**, 73-80 (2018). https://doi.org:10.1038/nmeth.4511

40 Muzumdar, M. D., Tasic, B., Miyamichi, K., Li, L. & Luo, L. A global double-fluorescent Cre reporter mouse. *Genesis : the journal of genetics and development.* **45**, 593-605 (2007). https://doi.org:10.1002/dvg.20335

41 Schulte, H., Mühlfeld, C. & Brandenberger, C. Age-Related Structural and Functional Changes in the Mouse Lung. *Frontiers in Physiology* **10** (2019). https://doi.org:10.3389/fphys.2019.01466

42 Janker, F., Weder, W., Jang, J.-H. & Jungraithmayr, W. Preclinical, non-genetic models of lung adenocarcinoma: a comparative survey. *Oncotarget* **9**, 30527-30538 (2018). https://doi.org:10.18632/oncotarget.25668

43 Sozio, F., Schioppa, T., Sozzani, S. & Del Prete, A. Urethane-induced lung carcinogenesis. *Methods in cell biology.* **163**, 45-57 (2021). https://doi.org:10.1016/bs.mcb.2020.09.005

44 Kizhakke Puliyakote, A. S. *et al.* Morphometric differences between central vs. surface acini in A/J mice using high-resolution micro-computed tomography. *Journal of Applied Physiology* **121**, 115-122 (2016). https://doi.org:10.1152/japplphysiol.00317.2016

45 Thiesse, J. *et al.* Lung structure phenotype variation in inbred mouse strains revealed through in vivo micro-CT imaging. *Journal of applied physiology.* **109**, 1960-1968 (2010). https://doi.org:10.1152/japplphysiol.01322.2009

46 Vasilescu, D. M. *et al.* Assessment of morphometry of pulmonary acini in mouse lungs by nondestructive imaging using multiscale microcomputed tomography. *Proceedings of the National Academy of Sciences* **109**, 17105-17110 (2012). https://doi.org:10.1073/pnas.1215112109

47 Vanderpool, R. R. & Chesler, N. C. Characterization of the Isolated, Ventilated, and Instrumented Mouse Lung Perfused with Pulsatile Flow. *Journal of Visualized Experiments* (2011). https://doi.org:10.3791/2690

48 Barbone, P. E. *et al.* Adjoint-weighted variational formulation for the direct solution of inverse problems of general linear elasticity with full interior data. *International journal for numerical methods in engineering* **81**, 1713-1736 (2010).
49 DOLFINx: The next generation FEniCS problem solving environment. (2023).
50 Bishop, C. M. Machine Learning. *Machine learning* **128** (2006).
51 Hastie, T., Tibshirani, R. & Friedman, J. H. *The Elements of Statistical Learning: Data Mining, Inference, and Prediction*. (Springer, 2009).
52 Pratt, M. J. Introduction to ISO 10303—the STEP Standard for Product Data Exchange. *Journal of Computing and Information Science in Engineering* **1**, 102-103 (2001). https://doi.org:10.1115/1.1354995
53 Berezvai, S. & Kossa, A. Closed-form solution of the Ogden–Hill's compressible hyperelastic model for ramp loading. *Mechanics of Time-Dependent Materials* **21**, 263-286 (2017). https://doi.org:10.1007/s11043-016-9329-5
54 Andrikakou, P., Vickraman, K. & Arora, H. On the behaviour of lung tissue under tension and compression. *Scientific Reports* **6**, 36642 (2016). https://doi.org:10.1038/srep36642
55 Vawter, D., Fung, Y. & West, J. Constitutive equation of lung tissue elasticity. (1979).
56 Shi, L. *et al.* Modeling the influence of gravity and the mechanical properties of elastin and collagen fibers on alveolar and lung pressure–volume curves. *Scientific Reports* **12** (2022). https://doi.org:10.1038/s41598-022-16650-0
57 Tawhai, M. H., Nash, M. P., Lin, C.-L. & Hoffman, E. A. Supine and prone differences in regional lung density and pleural pressure gradients in the human lung with constant shape. *Journal of Applied Physiology* **107**, 912-920 (2009).
58 Munson, B. R., Rothmayer, A. P. & Okiishi, T. H. *Fundamentals of Fluid Mechanics, 7th Edition*. (Wiley, 2012).
59 Mead, J., Takishima, T. & Leith, D. Stress distribution in lungs: a model of pulmonary elasticity. *Journal of applied physiology* **28**, 596-608 (1970).
60 Concha, F., Sarabia-Vallejos, M. & Hurtado, D. E. Micromechanical model of lung parenchyma hyperelasticity. *Journal of the mechanics and physics of solids.* **112**, 126-144 (2018). https://doi.org:10.1016/j.jmps.2017.11.021
61 Heinrich, M. P., Jenkinson, M., Brady, S. M. & Schnabel, J. A. in *Medical Image Computing and Computer-Assisted Intervention – MICCAI 2012* 115-122 (Springer Berlin Heidelberg, 2012).
62 Heinrich, M. P. *et al.* MIND: Modality independent neighbourhood descriptor for multi-modal deformable registration. *Medical image analysis.* **16**, 1423-1435 (2012). https://doi.org:info:doi/10.1016/j.media.2012.05.008
63 Holzapfel, G. A. *Nonlinear Solid Mechanics: A Continuum Approach for Engineering*. (Wiley, 2000).
64 Albocher, U., Oberai, A. A., Barbone, P. E. & Harari, I. Adjoint-weighted equation for inverse problems of incompressible plane-stress elasticity. *Computer methods in applied mechanics and engineering* **198**, 2412-2420 (2009). https://doi.org:10.1016/j.cma.2009.02.034
65 Jorba, I. *et al.* Nonlinear elasticity of the lung extracellular microenvironment is regulated by macroscale tissue strain. *Acta Biomaterialia* **92**, 265-276 (2019). https://doi.org:10.1016/j.actbio.2019.05.023

66 Polio, S. R. *et al.* Cross-platform mechanical characterization of lung tissue. *PLOS ONE* **13**, e0204765 (2018). https://doi.org:10.1371/journal.pone.0204765
67 Perlman, C. E. & Wu, Y. In situ determination of alveolar septal strain, stress and effective Young's modulus: an experimental/computational approach. *American Journal of Physiology-Lung Cellular and Molecular Physiology* **307**, L302-L310 (2014). https://doi.org:10.1152/ajplung.00106.2014
68 In'T Veld, P. J. & Stevens, M. J. Simulation of the Mechanical Strength of a Single Collagen Molecule. *Biophysical Journal* **95**, 33-39 (2008). https://doi.org:10.1529/biophysj.107.120659
69 Fratzl, P. Collagen: Structure and Mechanics, an Introduction. (2008). https://doi.org:10.1007/978-0-387-73906-9_1
70 Boyce, M. C. & Arruda, E. M. Constitutive Models of Rubber Elasticity: A Review. *Rubber chemistry and technology* **73**, 504-523 (2000). https://doi.org:10.5254/1.3547602
71 Holzapfel, G. A. & Simo, J. C. Entropy elasticity of isotropic rubber-like solids at finite strains. *Computer methods in applied mechanics and engineering* **132**, 17-44 (1996). https://doi.org:10.1016/0045-7825(96)01001-8
72 Treloar, L. R. G. The mechanics of rubber elasticity. *Journal of polymer science.* **48**, 107-123 (1974). https://doi.org:10.1002/polc.5070480110
73 Treloar, L. R. G. *The physics of rubber elasticity*. 3rd edn, (Clarendon Press, 2005).
74 James, H. M. & Guth, E. Theory of the Elasticity of Rubber. *Journal of Applied Physics* **15** (1944/04/01). https://doi.org:10.1063/1.1707432
75 Beatty, M. F. Topics in finite elasticity: hyperelasticity of rubber, elastomers, and biological tissues—with examples. (1987).
76 Halvorsen, S., Wang, R. & Zhang, Y. Contribution of Elastic and Collagen Fibers to the Mechanical Behavior of Bovine Nuchal Ligament. *Annals of Biomedical Engineering* **51**, 2204-2215 (2023). https://doi.org:10.1007/s10439-023-03254-6
77 Sherman, V. R., Yang, W. & Meyers, M. A. The materials science of collagen. *Journal of the mechanical behavior of biomedical materials.* **52**, 22-50 (2015). https://doi.org:10.1016/j.jmbbm.2015.05.023
78 Suki, B. & Bates, J. H. T. Lung tissue mechanics as an emergent phenomenon. *Journal of applied physiology.* **110**, 1111-1118 (2011). https://doi.org:10.1152/japplphysiol.01244.2010
79 Maksym, G. N., Fredberg, J. J. & Bates, J. H. T. Force heterogeneity in a two-dimensional network model of lung tissue elasticity. *Journal of applied physiology.* **85**, 1223-1229 (1998). https://doi.org:10.1152/jappl.1998.85.4.1223
80 Cavalcante, F. S. A. *et al.* Mechanical interactions between collagen and proteoglycans: implications for the stability of lung tissue. *Journal of applied physiology.* **98**, 672-679 (2005). https://doi.org:10.1152/japplphysiol.00619.2004
81 Sarabia-Vallejos, M. A., Zuñiga, M. & Hurtado, D. E. The role of three-dimensionality and alveolar pressure in the distribution and amplification of alveolar stresses. *Scientific reports.* **9** (2019). https://doi.org:10.1038/s41598-019-45343-4
82 Mariano, C. A. *et al.* Novel Mechanical Strain Characterization of Ventilated ex vivo Porcine and Murine Lung using Digital Image Correlation. *Frontiers in Physiology* **11** (2020). https://doi.org:10.3389/fphys.2020.600492

83 Mariappan, Y. K. *et al.* Estimation of the absolute shear stiffness of human lung parenchyma using ¹H spin echo, echo planar MR elastography. *Journal of Magnetic Resonance Imaging* **40**, 1230-1237 (2014). https://doi.org:10.1002/jmri.24479

84 Sicard, D. *et al.* Aging and anatomical variations in lung tissue stiffness. *American Journal of Physiology-Lung Cellular and Molecular Physiology* **314**, L946-L955 (2018). https://doi.org:10.1152/ajplung.00415.2017

85 West, J. B. & Luks, A. M. *West's Respiratory Physiology*. (Lippincott Williams & Wilkins, 2020).

86 Lee, G. C., Tseng, N. T. & Yuan, Y. M. Finite element modeling of lungs including interlobar fissures and the heart cavity. *Journal of biomechanics.* **16**, 679-690 (1983). https://doi.org:10.1016/0021-9290(83)90078-7

87 Marinelli, J. P. *et al.* Quantitative assessment of lung stiffness in patients with interstitial lung disease using MR elastography. *Journal of Magnetic Resonance Imaging* **46**, 365-374 (2017). https://doi.org:10.1002/jmri.25579

Supplementary Materials

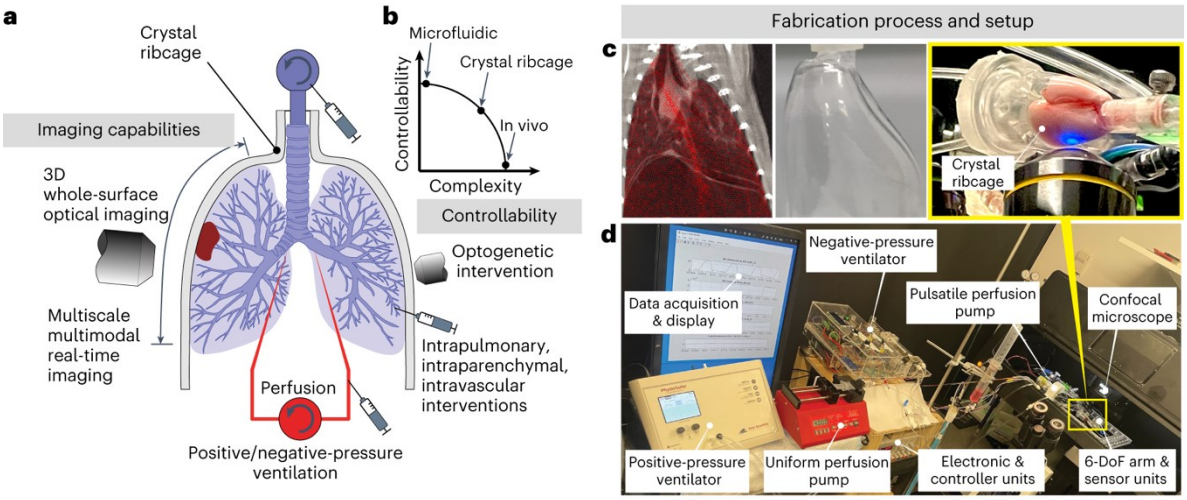

Figure S1 | Illustration of the crystal ribcage platform. This figure reproduces panels (a-d) from Figure 1 in our earlier work[36] and depicts the details of the crystal ribcage platform. The panels are as follows: (a) Schematic of the lung within the crystal ribcage, depicting the imaging, controllability, and intervention capabilities of the platform, (b) The crystal ribcage supports the same imaging capabilities and controllability of organ-on-chip models, while maintaining the complex environment of *in vivo* lungs, (c) Age- and strain-specific microCT scans are used to fabricate the crystal ribcage through a multistep fabrication process, in which the geometry is derived from microCT images, and (d) The portable platform to maintain, monitor and record the lung physiological condition during real-time imaging.

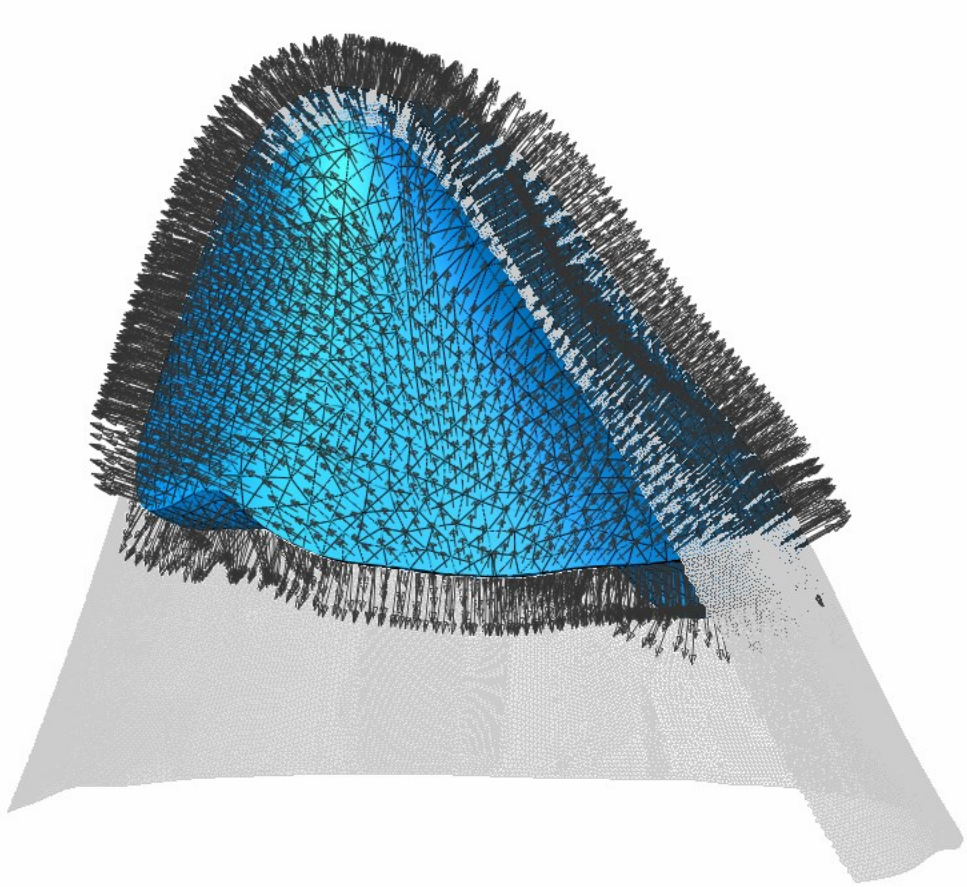

Figure S2 | The boundary conditions on the finite-element model. In the simulation, the lung (blue part) is constrained to slide frictionlessly along the surface of the rigid ribcage (gray surface). A negative pressure load (black vectors) is applied to the surface of the lung in order to emulate negative transpulmonary pressure. Part of the virtual ribcage has been visually hidden to show the lung below.

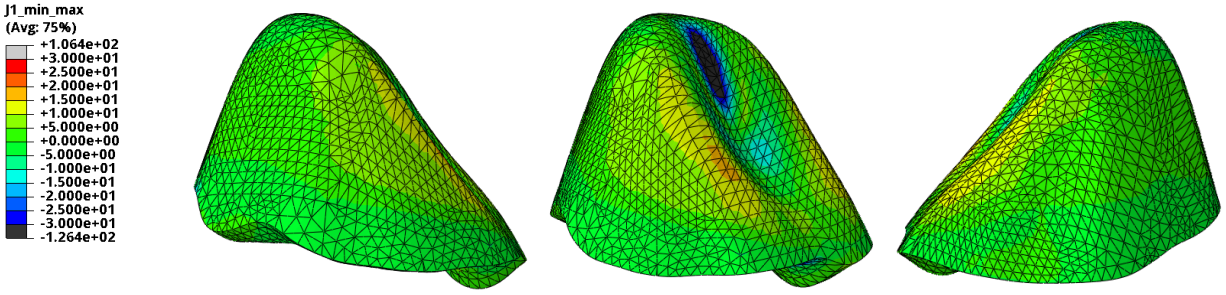

Figure S3 | Demonstrating the percent error in our pseudo-3D approximation of the Jacobian determinant when solving the inverse problem. These panels show the percent error of $(\lambda_1\lambda_2)^{1.5}$ relative to the true Jacobian $\lambda_1\lambda_2\lambda_3$. We see that the approximation is generally accurate to within 5-15% error across the majority of the lung's surface.

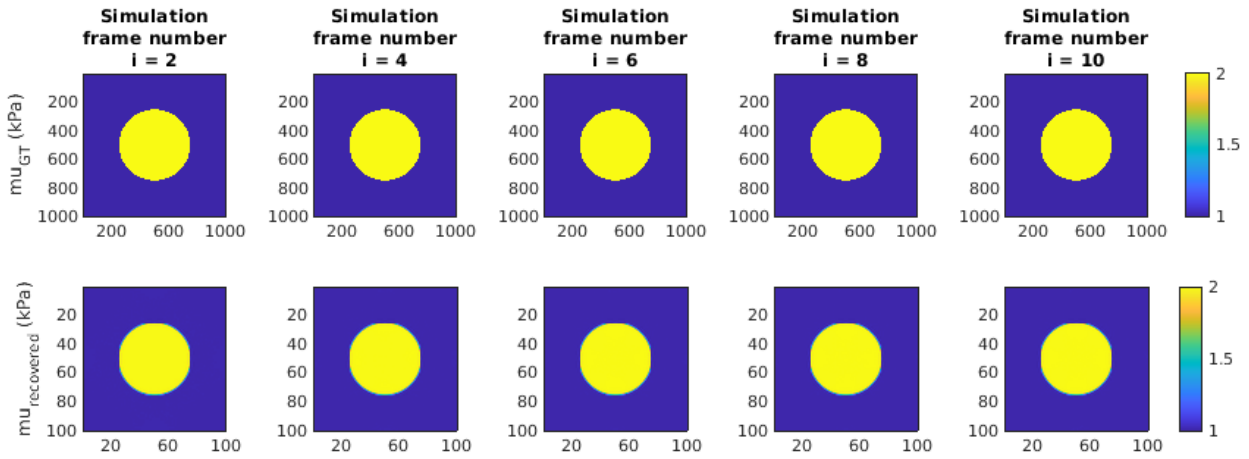

Figure S4 | Validating the nonlinear inverse solver on a simple, pseudo-3D, hyperelastic foam membrane. In Abaqus, we construct a 2D, hyperelastic foam membrane having a shear modulus of 2 kPa within a circular inclusion and having a shear modulus of 1 kPa outside the inclusion. We then stretch the model by 10% along the two directions parallel to the edges of the domain. The first row shows the ground-truth shear modulus distribution, while the second row provides the shear-modulus distribution estimated from the simulated total displacements and the nonlinear formulation of the inverse solver.

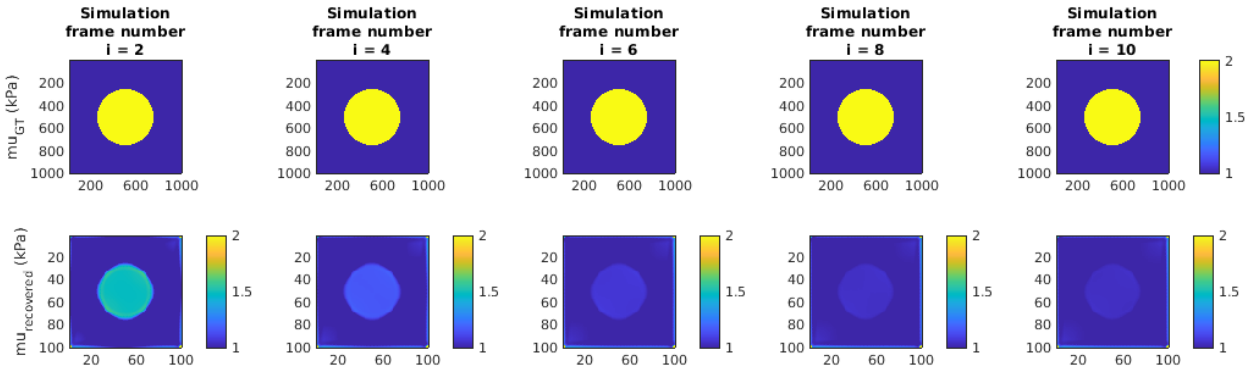

Figure S5 | Assessing the piecewise-linear inverse solver on a simple, pseudo-3D, hyperelastic foam membrane. In Abaqus, we construct a 2D, hyperelastic foam membrane having a shear modulus of 2 kPa within a circular inclusion and having a shear modulus of 1 kPa outside the inclusion. We then stretch the model by 10% along the two directions parallel to the edges of the domain. The first row shows the ground-truth shear modulus distribution, while the second row provides the shear-modulus distribution estimated from the simulated incremental displacements and the piecewise-linear formulation of the inverse solver.

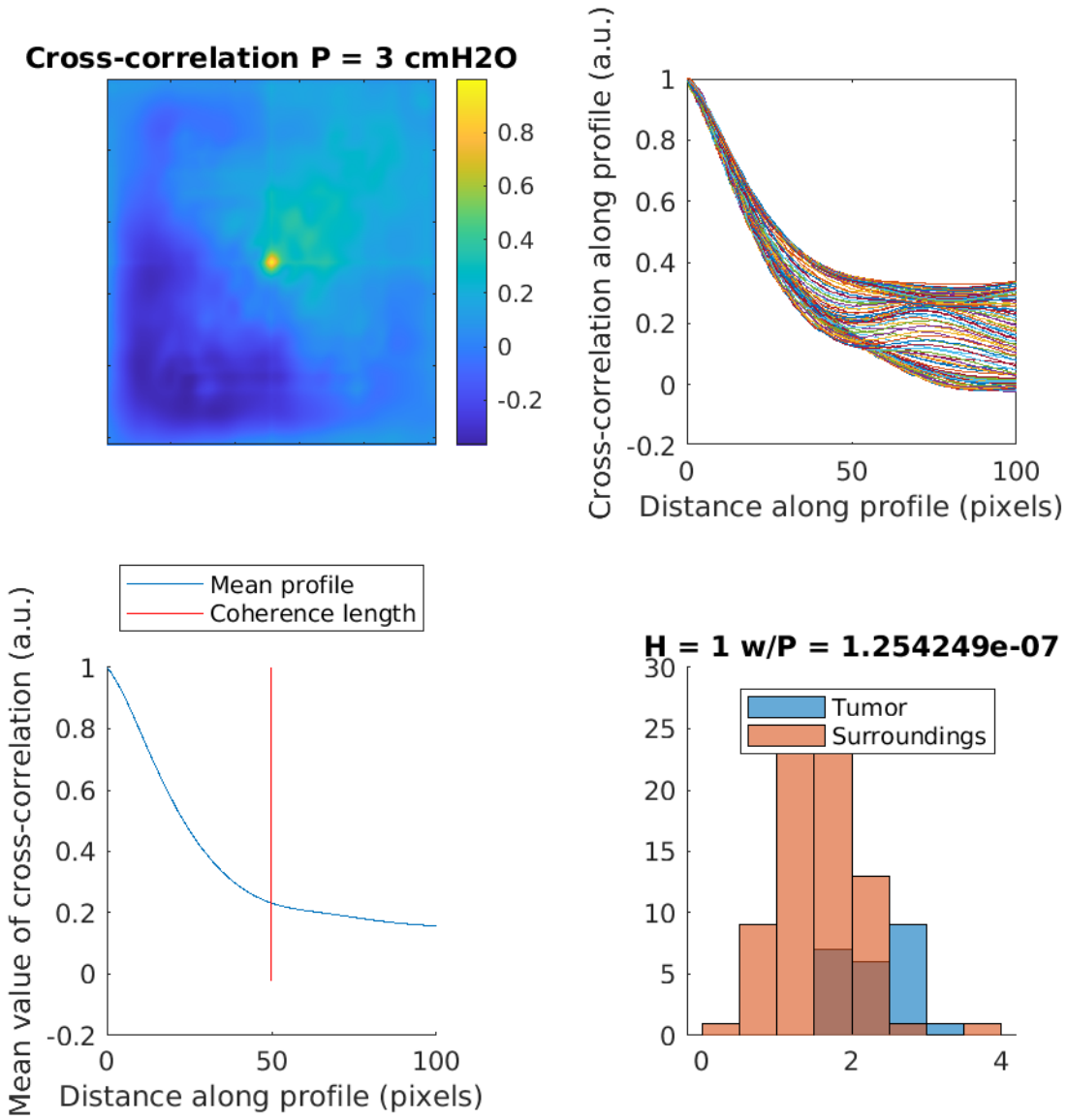

Figure S6 | Determining the coherence length for statistically comparing mappings. (Top left) Normalized autocorrelation of the estimated stiffnesses for the lung with cancer (Fig. 5). (Top right) 100 profiles of the autocorrelation decay with the magnitude of the displacement of the copy of the original mapping. (Bottom left) The mean profile begins to plateau when the distance between the field and its displaced copy reaches 50 pixels, indicating that 50x50 patches within the image are mutually independent. (Bottom right) The histogram of the stiffnesses within the tumor and the surroundings after discretization of the stiffness mapping into 50x50 pixel patches. The difference between these distributions is statistically significant with a p-value of 1.25e-7.

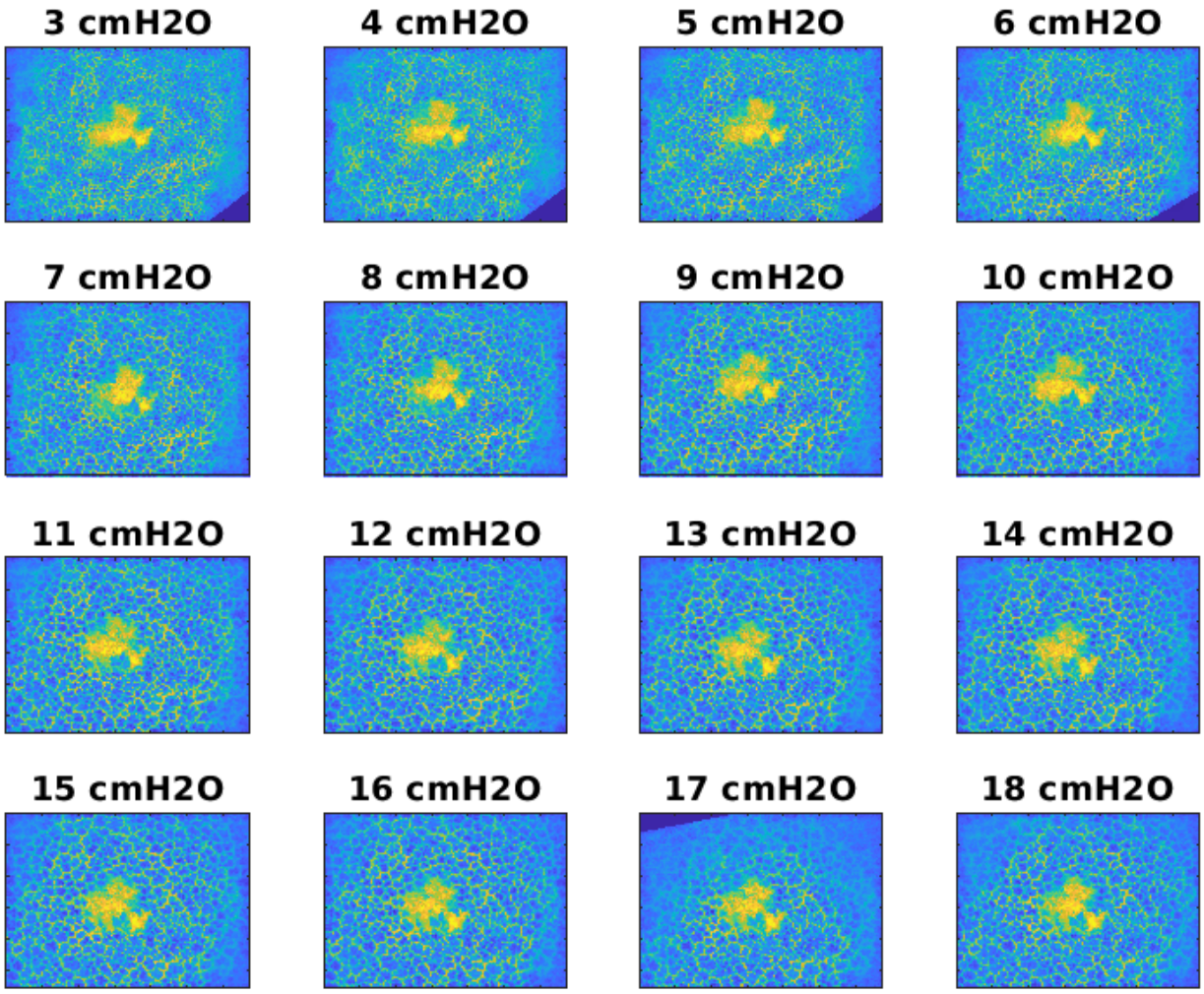

Figure S7 | Images of the lung from 2 cmH_2O to 18 cmH_2O. During the course of our experiments, we collect images of the lung at pressures incrementing from 2 cmH_2O to 18 cmH_2O in increments of 1 cmH_2O.

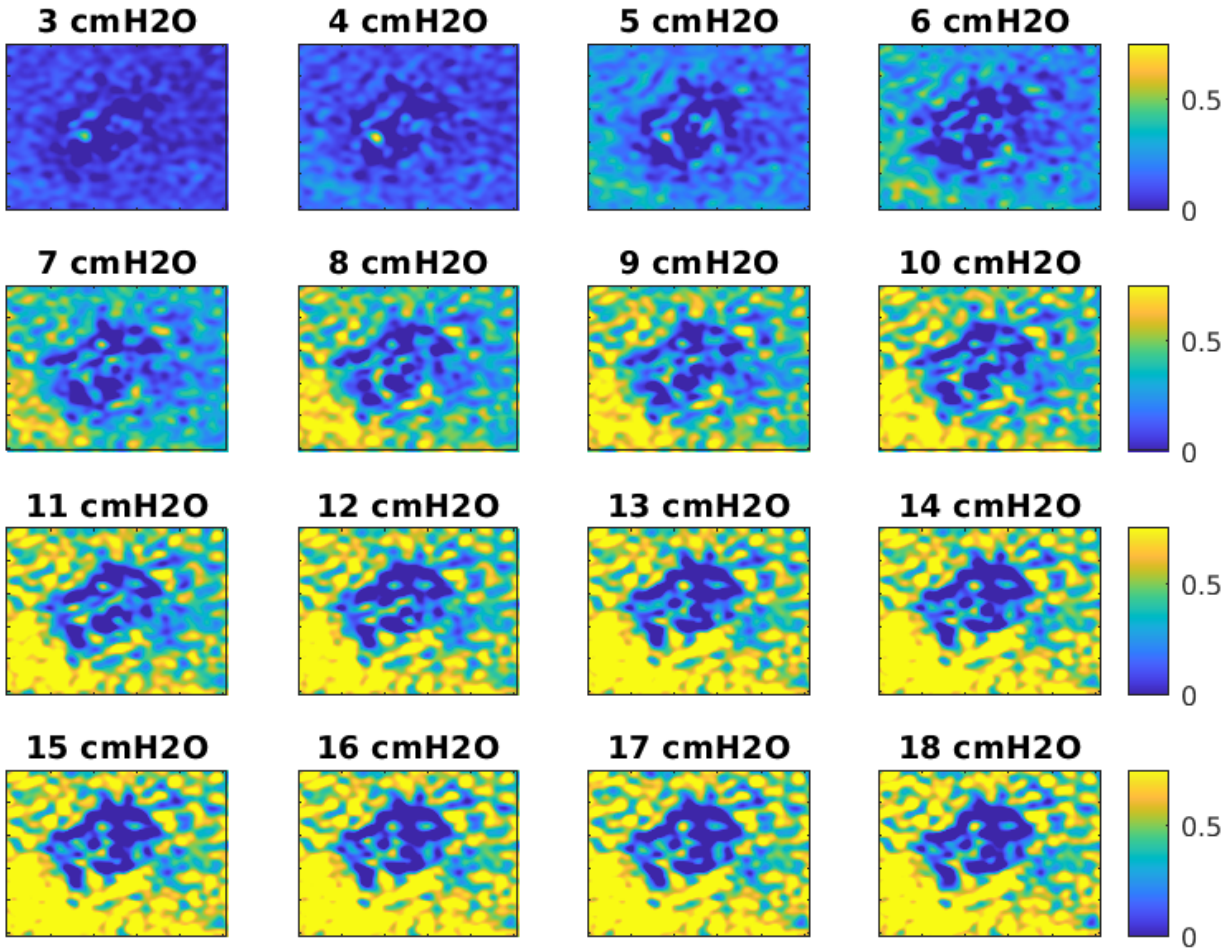

Figure S8 | Strain maps from 2 cmH_2O to 18 cmH_2O. We register images of the lung between consecutive pressures and then compose the resulting displacement mappings. From the composed displacement mappings, we compute the total areal strain throughout the domain at each pressure.

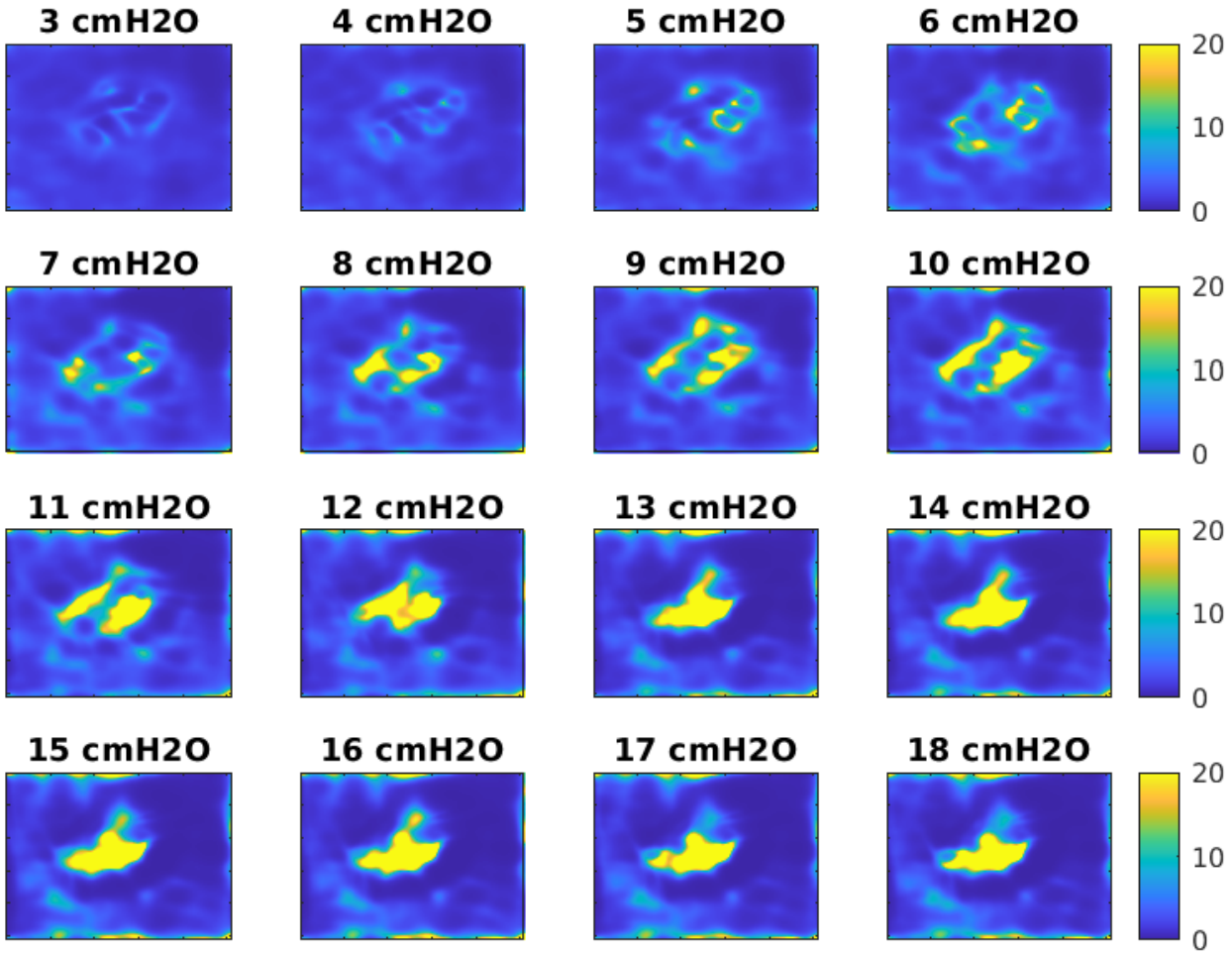

Figure S9 | Stiffness maps from 2 cmH_2O to 18 cmH_2O. From the registered displacements, we also solve the inverse elasticity problem for the stiffnesses throughout the domain at each pressure.

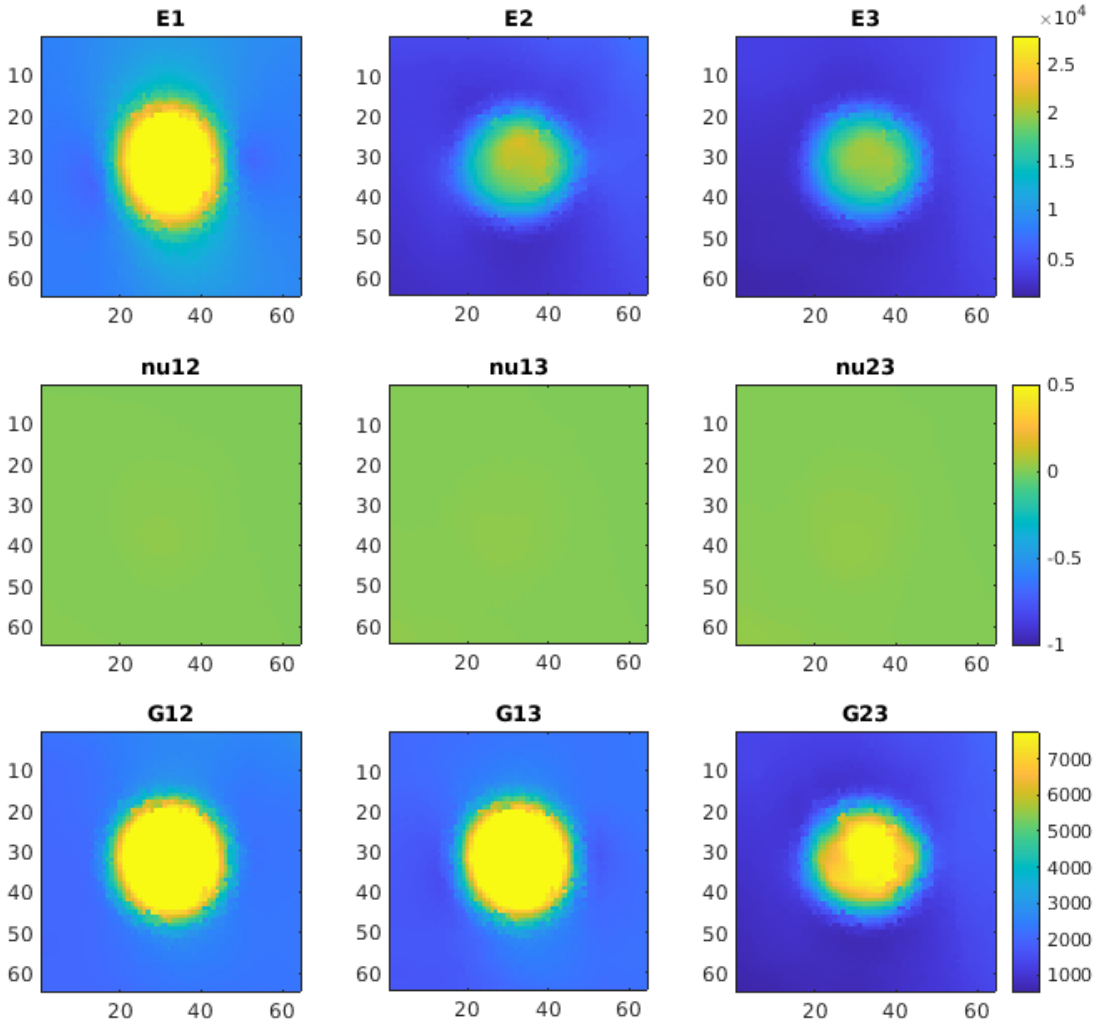

Figure S10 | The ground-truth, orthotropic stiffness of the finite-element model at 18 cmH_2O. As shown in Fig. 3, we simulated distension of the finite-element model containing a stiff inclusion representing a cancerous tumor. Here, we show the ground-truth coefficients characterizing the elasticity tensor at 18 cmH_2O for comparison to the stiffness maps in S10 and S11. Units of the elasticity moduli and the shear moduli are in Pascals, while the Poisson ratios are unitless.

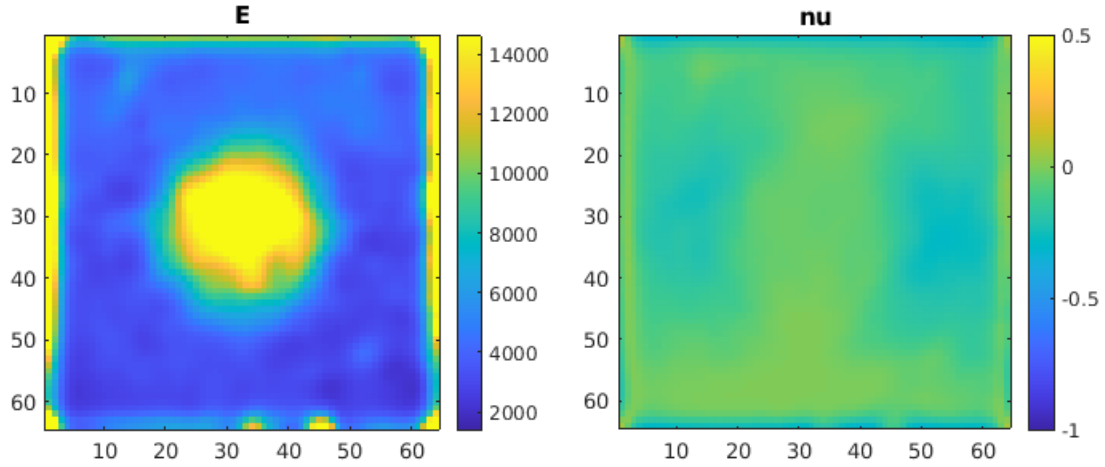

Figure S11 | The isotropic stiffness of the finite-element model at 18 cmH_2O. As shown in Fig. 3, we simulated distension of the finite-element model containing a stiff inclusion representing a cancerous tumor. Here, we show the estimates isotropic coefficients approximating the elasticity tensor at 18 cmH_2O. Units of the elastic modulus are Pascals, while the Poisson ratio is unitless.

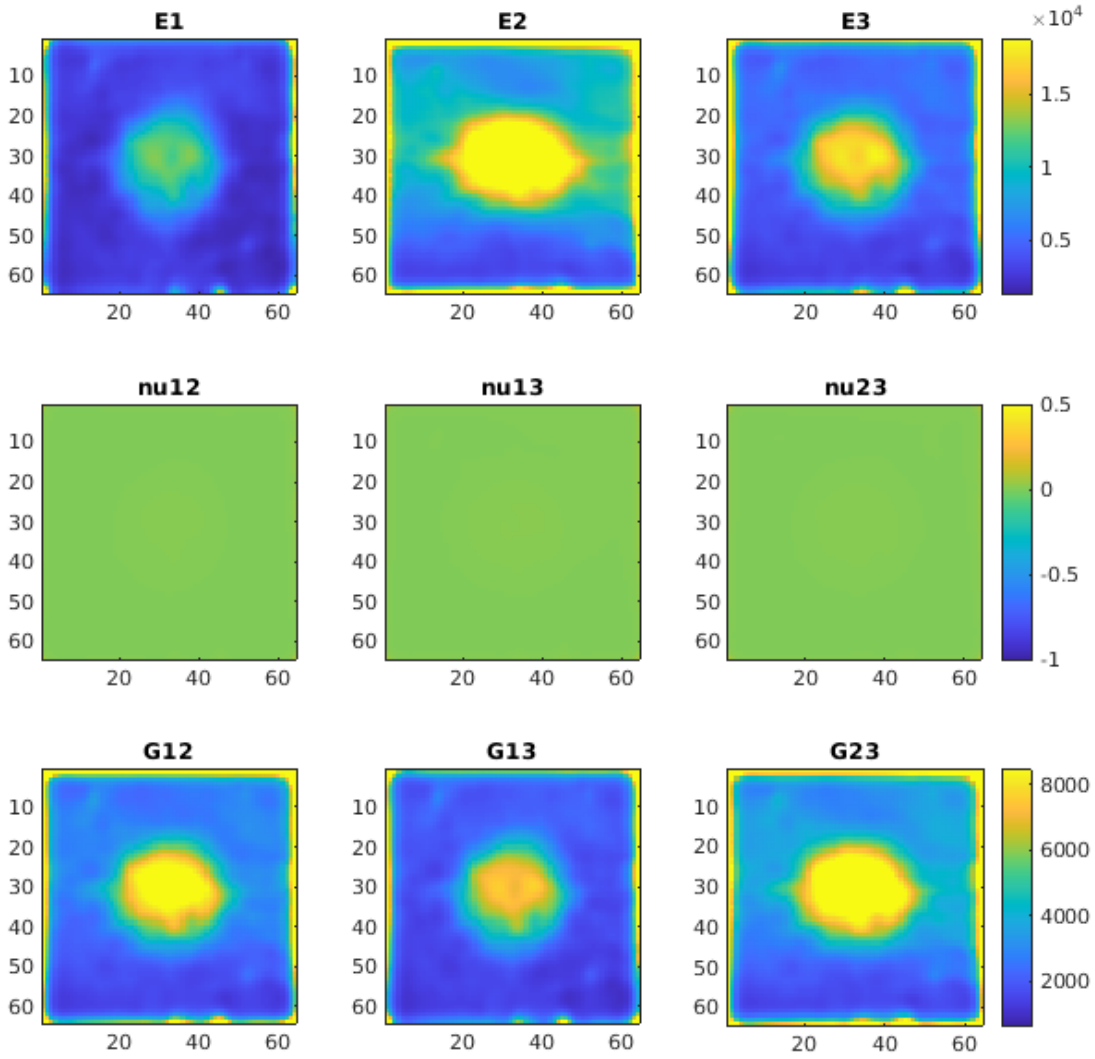

Figure S12 | The estimated, orthotropic stiffness of the finite-element model at 18 cmH_2O. As shown in Fig. 3, we simulated distension of the finite-element model containing a stiff inclusion representing a cancerous tumor. Here, we show the estimated orthotropic coefficients of the elasticity tensor at 18 cmH_2O. Units of the elastic moduli and the shear moduli are in Pascals, while the Poisson ratios are unitless.